

## RESEARCH ARTICLE

10.1002/2016JA023222

## Special Section:

Geospace system responses to the St. Patrick's Day storms in 2013 and 2015

## Key Points:

- Geospace characterization of Saint Patrick's Day storm over Southeast Asia with a multiinstrumental approach is provided
- Postsunset scintillation inhibition has been detected and compared with the morphology and dynamics of the ionospheric F layer
- Meridional and zonal variations between the equatorial ionospheric anomaly crests are discussed in depth

## Correspondence to:

L. Spogli,  
luca.spogli@ingv.it

## Citation:

Spogli, L., et al. (2016), Formation of ionospheric irregularities over Southeast Asia during the 2015 St. Patrick's Day storm, *J. Geophys. Res. Space Physics*, 121, 12,211–12,233, doi:10.1002/2016JA023222.

Received 25 JUL 2016

Accepted 16 NOV 2016

Accepted article online 20 NOV 2016

Published online 29 DEC 2016

## Formation of ionospheric irregularities over Southeast Asia during the 2015 St. Patrick's Day storm

Luca Spogli<sup>1,2</sup> , Claudio Cesaroni<sup>1</sup>, Domenico Di Mauro<sup>1</sup>, Michael Pezzopane<sup>1</sup>, Lucilla Alfonsi<sup>1</sup>, Elvira Musico<sup>1,3</sup> , Gabriella Povero<sup>4</sup> , Marco Pini<sup>4</sup>, Fabio Dovis<sup>5</sup> , Rodrigo Romero<sup>5</sup>, Nicola Linty<sup>5</sup> , Prayitno Abadi<sup>6</sup> , Fitri Nuraeni<sup>6</sup>, Asnawi Husin<sup>6</sup>, Minh Le Huy<sup>7</sup>, Tran Thi Lan<sup>7</sup>, The Vinh La<sup>8</sup>, Valdir Gil Pillat<sup>9</sup>, and Nicolas Floury<sup>10</sup>

<sup>1</sup>Istituto Nazionale di Geofisica e Vulcanologia, Rome, Italy, <sup>2</sup>SpacEarth Technology, Rome, Italy, <sup>3</sup>Department of Information, Electronics and Telecommunications, Sapienza University of Rome, Rome, Italy, <sup>4</sup>Istituto Superiore Mario Boella, Turin, Italy, <sup>5</sup>Department of Electronics and Telecommunications, Politecnico di Torino, Turin, Italy, <sup>6</sup>National Institute of Aeronautics and Space LAPAN, Bandung, Indonesia, <sup>7</sup>Institute of Geophysics Vietnam Academy of Science and Technology, Hanoi, Vietnam, <sup>8</sup>NAVIS Centre, Hanoi University of Science and Technology, Hanoi, Vietnam, <sup>9</sup>Física e Astronomia, Universidade do Vale do Paraíba, São José dos Campos, Brazil, <sup>10</sup>European Space Agency, Noordwijk, Netherlands

**Abstract** We investigate the geospace response to the 2015 St. Patrick's Day storm leveraging on instruments spread over Southeast Asia (SEA), covering a wide longitudinal sector of the low-latitude ionosphere. A regional characterization of the storm is provided, identifying the peculiarities of ionospheric irregularity formation. The novelties of this work are the characterization in a broad longitudinal range and the methodology relying on the integration of data acquired by Global Navigation Satellite System (GNSS) receivers, magnetometers, ionosondes, and Swarm satellites. This work is a legacy of the project Equatorial Ionosphere Characterization in Asia (ERICA). ERICA aimed to capture the features of both crests of the equatorial ionospheric anomaly (EIA) and trough (EIT) by means of a dedicated measurement campaign. The campaign lasted from March to October 2015 and was able to observe the ionospheric variability causing effects on radio systems, GNSS in particular. The multiinstrumental and multiparametric observations of the region enabled an in-depth investigation of the response to the largest geomagnetic storm of the current solar cycle in a region scarcely reported in literature. Our work discusses the comparison between northern and southern crests of the EIA in the SEA region. The observations recorded positive and negative ionospheric storms, spread *F* conditions, scintillation enhancement and inhibition, and total electron content variability. The ancillary information on the local magnetic field highlights the variety of ionospheric perturbations during the different storm phases. The combined use of ionospheric bottomside, topside, and integrated information points out how the storm affects the *F* layer altitude and the consequent enhancement/suppression of scintillations.

### 1. Introduction

Different regions of the Earth's ionosphere present specific peculiarities when subject to a geomagnetic storm. Actually, it is known that ionospheric features vary with both latitude and longitude, making the effect of a given storm not equally distributed around the Earth and variable on large time and space scale ranges [Basu et al., 2002; Kintner et al., 2009]. This is mainly due to the morphology of the Earth's magnetic field, which makes the equatorial, polar, and auroral regions more exposed to the formation of the ionospheric irregularities. In this work, we concentrate our analysis on the equatorial ionosphere, where the so-called equatorial ionospheric anomaly (EIA) and trough (EIT) take place. The EIA forms where the Earth's magnetic field *B* is approximately parallel to the surface. During daytime, the dynamo electric field which characterizes the ionospheric *E* layer, is eastward. Because of the  $E \times B$  drift, the *F* layer ionospheric plasma undergoes an uplift at the magnetic equator. The plasma falls back down under pressure gradient and gravity. The result of such interplay is the formation of the EIA, which is characterized by a minimum of the ionization at the magnetic equator (named EIT) and two maxima, located at about  $\pm 15^\circ/20^\circ$  in magnetic latitude off the magnetic equator. Such maxima are known as crests of the EIA. Before sunset, the ionospheric *E* layer is characterized by a decrease of both the plasma density and the dynamo electric field, thus resulting in an overall weakening of the EIA. At the same time, the ionospheric *F* layer is characterized by the appearance of a dynamo leading to an overall enhancement of the eastward electric field [Rishbeth, 1971].

The interplay between all postsunset ionospheric phenomena leads to a further, rapid uplifting of the  $F$  layer, a consequent intensification of the crests of the EIA and, above all, to the formation of a Rayleigh-Taylor instability (RTI) [see, e.g., Jin *et al.*, 2008]. The plasma cascade, characterizing the RTI, drives the formation of plasma density irregularities in a wide range of scale sizes. Large electron density depletions are typically lengthened along the  $B$  field lines and are commonly called “ionospheric plasma bubbles” [see, e.g., Young *et al.*, 1984]. Smaller-scale irregularities, generally below the Fresnel’s scale (i.e., about few hundred meters for L-band signals), are produced by a plasma cascade mechanism and are typically embedded into the ionospheric plasma bubbles. The latter, referred worldwide as “small-scale irregularities,” are a threat to the reliability of transionospheric signals [Wernik and Liu, 1974]. From a Global Navigation Satellite System (GNSS) point of view, L-band signals experience diffraction when encountering ionospheric irregularities. The overall effect is that, when received at ground, GNSS signals can fluctuate in phase and amplitude, producing a so-called “ionospheric scintillation.” The induced amplitude fading can exceed 20 dB at low latitudes [Basu *et al.*, 2002], posing a serious threat, for instance, on the services relying on GNSS technology.

Moreover, irregularities and inhomogeneities present in the ionospheric  $F$  layer are responsible for the spread that often characterizes the trace of ionograms recorded by ionosondes located at low latitude. Such effect was identified in the 1930s [see, e.g., Booker and Wells, 1938], and it is commonly called “spread  $F$ .” When present, it impedes a reliable scaling of ionograms, but, at the same time, it provides information about the irregularities in the  $F$  region. The equatorial spread  $F$  (ESF) typically takes place in the local postsunset hours, and the scale sizes of the irregularities driving ESF vary from centimeters up to few hundreds of kilometers. The ESF is usually characterized into two main categories: the range (RSF) and the frequency spread  $F$  (FSF) [Piggott and Rawer, 1972]. In the literature, further subdivisions can also be found [Chen *et al.*, 2006], but in the present work we refer to RSF and FSF only. The occurrence of ESF depends on the geographical sector, the time of the day, season, and solar and geomagnetic activities [Kelley, 2009].

Besides the EIA, the Southeast Asian (SEA) ionosphere is characterized by a particularly intense equatorial electrojet [Amory-Mazaudier *et al.*, 2006]. The equatorial electrojet (EEJ) is an electric current of very high density that flows in a latitudinal narrow zone of approximately  $6^\circ$  in width centered above the magnetic dip equator. The EEJ flows eastward during the daytime hours, especially around local noon, at a mean altitude of about 100 km. The EEJ drives a meaningful increase of the diurnal variation in the horizontal component of  $B$  measured at ground, at the magnetic equator, and its vicinity. As the EEJ strongly modulates the daily variation of  $B$ , a regional characterization of low-latitude ionosphere is the most effective way to highlight the complex cause-effect mechanisms of a storm development. The relationship between EEJ and EIA has been verified by means of total electron content (TEC) data derived from GNSS receivers in the Indian sector during year 2006 [Jose *et al.*, 2011].

As for the peculiarities of the EEJ over SEA, we investigate the EIA evolution to draw the geospace response near the two crests, where TEC gradients mostly occur often jeopardizing the transionospheric satellite signals. The possibility to predict the evolution of TEC gradients could significantly help the resilience of GNSS-based operations against severe space weather events.

The multiinstrumental and multidisciplinary methodology here presented was made possible by the coordinated measurement campaign carried out within the project Equatorial Ionosphere Characterization in Asia (ERICA) [Povero *et al.*, 2015]. ERICA was funded by the European Space Agency to characterize the features of EIA and EIT over SEA by leveraging on a dedicated campaign of magnetic and ionospheric measurements. The ERICA network counted GNSS receivers, ionosondes, and magnetometers, owned by the Indonesian National Institute of Aeronautics and Space and by the Institute of Geophysics of the Vietnamese Academy of Science and Technology. The campaign carried out during ERICA lasted from 1 March to 9 October 2015; thus, it was able to detect the St. Patrick’s Day storm. Such a network allowed a multi-instrumental description of the ionospheric response to the disturbances induced by the St. Patrick’s Day storm over SEA, providing a detailed picture of the local aspects, as opposed to recent papers mainly dealing with global observations [Astafyeva *et al.*, 2015b; Nava *et al.*, 2016; Carter *et al.*, 2016; Nayak *et al.*, 2016]. Moreover, a comparison between northern and southern crests of the EIA in the SEA region is also given here for the first time by means of ground measurements. Additional to the data from ERICA network, data made available by the International GPS Service (IGS) as well as data sets acquired by a Chinese ionosonde in Sanya are included

**Table 1.** Location of the GNSS Scintillation Receivers, Magnetometers, and Ionosondes

Location	Latitude (°N)	Longitude (°E)	Magnetic Latitude (°N)	Country	GNSS Scintillation	Magnetometer	Ionosonde
Phu Thuy	21.03	106.00°E	11.22	Vietnam	<b>X GSV4004</b>	<b>X</b>	Not present
Sanya	18.34	109.62	8.54	China	Not present	Not present	<b>X Digisonde</b>
Hue	16.40	107.60	6.61	Vietnam	<b>X GSV4004</b>	Not present	Not present
Da Lat	11.95	108.48	2.19	Vietnam	Not present	<b>X</b>	Not present
Manado	1.34	124.82	-7.91	Indonesia	<b>X GPStation 6</b>	Not present	Not present
Pontianak	-0.03	109.33	-9.71	Indonesia	<b>X GSV4004</b>	Not present	Not present
Bandung	-6.89	107.59	-16.53	Indonesia	<b>X GPStation 6</b>	Not present	Not present
Pameungpeuk	-7.65	107.69	-17.29	Indonesia	Not present	<b>X</b>	Not present
Watakosek	-7.57	112.68	-17.17	Indonesia	Not present	<b>X</b>	Not present
Kupang	-10.16	123.66	-19.38	Indonesia	<b>X GPStation 6</b>	Not present	X <b>CADI</b>

in the analysis. This allowed to complement the information by maximizing the instrumental coverage of the investigated area.

The St. Patrick’s Day storm is the most intense event that occurred during the current solar cycle: after the sudden storm commencement on 17 March 2015, it is characterized by a long recovery phase, lasting until the end of the month. The study of this severe storm offers a unique occasion to advance the knowledge about the relation between geomagnetic field variations and ionospheric irregularities leading to scintillation. To be specific, at low latitudes, a remarkable consequence of storms in the ionosphere is the “suppression” of the instability mechanisms that produce ionospheric irregularities, leading to the inhibition of both ESF and scintillation phenomena occurring daily in the postsunset hours. This is most likely induced by the dominant westward *E* field perturbations related with the penetration of the electric fields from the auroral latitudes under disturbed conditions of the geospace. Whether the ionospheric response to geospace perturbations will result in an exacerbation or in an inhibition of scintillation and ESF occurrence is one of the most intriguing, not completely understood issues of the ionospheric science [see, e.g., *Muella et al., 2010; Alfonsi et al., 2013; Tulasi Ram et al., 2016*]. The present paper represents an additional contribution that could help the scientific community in developing an effective ionospheric modeling.

The paper is structured as follows: section 2 describes the data used and the adopted analysis methods; section 3 illustrates a detailed picture of the St. Patrick’s Day storm drawn by means of the regional monitoring infrastructures described in section 2; and section 4 describes and discusses the results of the multi-instrumental analysis, with particular emphasis to the ionospheric scintillation (presence/inhibition) and its correspondence to the geospace variations. Conclusions are given in section 5.

## 2. Data and Methods

Tables 1 and 2 provide the complete list of sites, where the instrumentation used to carry out the analysis are located. In particular, Table 1 provides the details about GNSS receivers for scintillation monitoring, ground magnetometers, and ionosondes. Such instrumentation is included in the ERICA project network, except for the ionosonde in Sanya, China. Table 2 summarizes the IGS receivers used to support the analysis with TEC measurements. Data acquired by such receivers are supported by the Swarm constellation data [*Friis-Christensen et al., 2008*]. The Swarm mission is characterized by a very peculiar geometry

**Table 2.** Location of the IGS Receivers

Receiver ID	Latitude (°N)	Longitude (°E)
Bako	-6.49	106.85
Coco	-12.59	96.83
Cusv	13.74	100.53
Darw	-12.50	131.08
Jfng	30.52	114.49
Karr	-20.59	117.05
Kat1	-14.22	132.09
Lhaz	29.39	91.06
Ntus	1.35	103.68
Pbr2	11.64	92.71
Pbri	11.64	92.71
Pimo	14.38	121.04
Ptag	14.32	121.02
Ptgg	14.32	121.02
Tcms	24.48	120.59
Tnml	24.48	120.59
Wuhn	30.53	114.36
Xmis	10.27	105.41

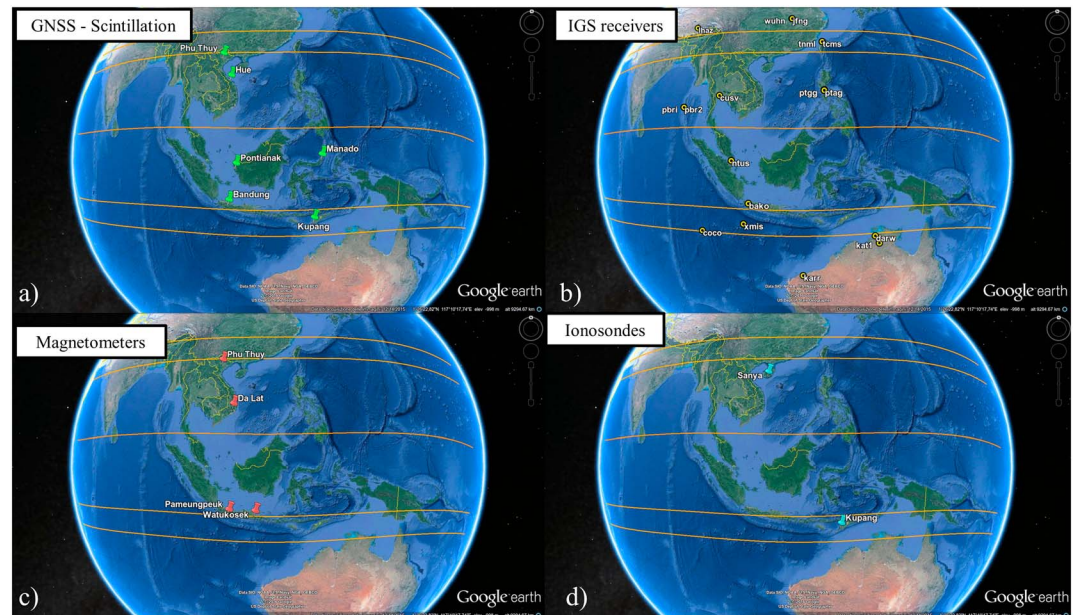


**Figure 1.** Location of the instrumentations used in the present work: (a) GNSS receivers for ionospheric scintillation monitoring (green pins), (b) IGS receivers (black/yellow circles), (c) ground magnetometers (red pins), and (d) ionosondes (light blue pins). The orange lines represent the position of the dip equator in March 2015 as measured by the Swarm constellation of satellites and the isoclinic lines at  $\pm 15^\circ$  and  $\pm 20^\circ$ .

of three satellites (Alpha, Bravo, and Charlie, hereafter A, B, and C), where satellites A and C fly side by side at a height of about 470 km, while satellite B flies at an altitude of about 530 km. Thus, the three satellites fly in the topside ionosphere. Additionally, their quasi-polar orbits allow for the coverage of the entire planet. All satellites are equipped with the same instruments, consisting of high-resolution sensors able to measure in situ the main features of geomagnetic and electric fields, plasma density, and temperature.

Figure 1 illustrates the position of the sites: GNSS receivers for ionospheric scintillation monitoring (Figure 1a, green pins), IGS receivers (Figure 1b, black/yellow circles), ground magnetometers (Figure 1c, red pins), and ionosondes (Figure 1d, light blue pins). In the figure, the orange lines represent the position of the dip equator in March 2015 as measured by the Swarm satellites and the isoclinic lines at  $\pm 15^\circ$  and  $\pm 20^\circ$ . Details about how dip equator and isoclinic lines are measured by Swarm are provided in section 2.2.2.

From the geographical distribution of the sites, it is possible to derive the following features of the network:

1. Even if the IGS receivers are not very dense in the considered region, their quite even distribution (Figure 1 b) allows for the coverage of most of the ionosphere over SEA;
2. The longitudinal sector centered at about  $106^\circ\text{E}$  is covered by the GNSS scintillation receivers in Phu Thuy, Hue, Pontianak, and Bandung (Figure 1a) and by all magnetometers (Figure 1c); this allows for the identification of symmetries and asymmetries between the northern and southern crests of the EIA in this sector;
3. The longitudinal sector centered at about  $124^\circ\text{E}$  is covered by the GNSS scintillation receivers in Manado and Kupang;
4. The magnetometers in Pameungpeuk and Watukosek (Figure 1c) are at the same latitude but at slightly different longitudes, which allows for the characterization of the longitudinal dependence of the geomagnetic field variations below the southern crest of the EIA;
5. The two ionosondes (Figure 1d) are located below the southern and northern crests of the EIA but in two different longitudinal sectors. In addition, the ionosonde in Kupang is co-located with a GNSS scintillation receiver, while the receiver closest to the Sanya ionosonde is that in Hue.

To identify the quiet behavior of the ionosphere, the analysis is performed over the days of March 2015 in which the  $K_p$  index is always lower than 3+ (days 3, 4, 5, 9, 10, 11, 12, 13, 14, 15, 26, 27, 28, 30, and 31). Other days of March are considered disturbed.

Details about the instrumentation, data, and adopted methods are provided in the following sections.

## 2.1. Ionospheric Data

### 2.1.1. GNSS Scintillation Data

As detailed in Table 1, two types of GNSS Ionospheric Scintillation and TEC Monitor receivers have been used: the GSV4004 (three stations) and the GPStation 6 (three stations). The GSV4004 is a multifrequency (L1, L2, and Satellite-Based Augmentation System (SBAS)) GPS receiver, widely used within the scientific community, while the most recent GPStation 6 is a multifrequency (L1, L2, L2C, L5, and SBAS) and multiconstellation (GPS, Galileo, and Global Navigation Satellite System) receiver. Both GSV4004 and GPStation 6 [Novatel, 2012] are able to calculate, starting from 50 Hz postcorrelation measurements of the GNSS signal, the widely adopted phase, and amplitude scintillation indices in near real time [Van Dierendonck *et al.*, 1993]. As concerns scintillations, in this paper we concentrated on the amplitude scintillation index only ( $S_4$ ), which is calculated every minute for each satellite in view by the given receiver. The GSV4004 provides  $S_4$  calculated on L1 only, while the GPStation 6 provides  $S_4$  for all available frequencies. To be consistent among all kind of receivers, only  $S_4$  values derived by GPS L1 signal are used in the present work. Furthermore, an elevation angle mask of  $30^\circ$  has been considered. To be compliant with the data analysis approach adopted by Spogli *et al.* [2013a, 2013b] and Alfonsi *et al.* [2013], the  $S_4$  index is projected to the vertical so as to minimize the effect of the geometry of the GNSS network. This  $S_4^{\text{vert}}$  is obtained by the following formula:

$$S_4^{\text{vert}} = S_4^{\text{slant}} / (F(\alpha_{\text{elev}}))^{\frac{p+1}{4}}, \quad (1)$$

where  $S_4^{\text{slant}}$  is the amplitude scintillation index derived by the receivers,  $p$  is the phase spectral slope, and  $F(\alpha_{\text{elev}})$  is the obliquity factor introduced by Mannucci *et al.* [1993] and defined as

$$F(\alpha_{\text{elev}}) = \frac{1}{\sqrt{1 - \left(\frac{R_E \cos \alpha_{\text{elev}}}{R_E + H_{\text{IPP}}}\right)^2}}. \quad (2)$$

In equation (2),  $R_E$  is the radius of the Earth and  $H_{\text{IPP}}$ , IPP being the ionospheric piercing point, is set to 350 km.

The assumptions behind the verticalization are

1. weak scattering regime, which allows the use of formula (31) of Rino [1979] to derive equation (1), and
2. single-phase screen approximation, which allows writing the exponent of the obliquity factor in formula (1) as  $\frac{p+1}{4}$ .

The firmware of GPStation 6 provides every minute the slope of the phase spectrum  $p$  in addition to the value of  $S_4$ ; thus,  $S_4^{\text{vert}}$  can be calculated easily. Conversely, for GSV4004 some extra assumptions are needed. By following the recommendations of Wernik *et al.* [2003], a value of  $p = 2.6$  introduced by Spogli *et al.* [2009] has been adopted, which makes the exponent in equation (1) equal to 0.9. A detailed discussion about the validity of such assumptions is detailed in Spogli *et al.* [2013b]. Hereafter, we refer to  $S_4^{\text{vert}}$  as  $S_4$ .

In order to provide as well a statistical and climatological picture of the scintillation phenomenon in the period covering the St. Patrick's Day storm, the Ground-Based Scintillation Climatology (GBSC) tool has been used to analyze amplitude scintillation data. The GBSC is a data analysis tool that was developed to provide a mapping of the ionospheric irregularities inducing scintillations over long-term periods and over selected areas [Spogli *et al.*, 2009; Alfonsi *et al.*, 2011a]. GBSC provides maps of the mean values, standard deviations, and percentage of occurrence above user-defined threshold of the parameters provided by GNSS scintillation monitoring receivers. Maps can be expressed in several coordinate systems, including geographic coordinates, geomagnetic coordinates, horizontal coordinates, universal time, local time, or magnetic local time.

### 2.1.2. GNSS TEC Data

In order to support the assessment of the ionospheric electron density distribution, data from IGS receivers installed in the area of interest (Figure 1b) are used as well. In particular, IGS receiver-independent exchange (RINEX) files containing GPS code and carrier phase observables acquired every 30 s from 09 to 26 March 2015 are used to obtain calibrated vertical TEC (vTEC) at each IPP applying the technique detailed in Ciraolo *et al.* [2007] and Cesaroni *et al.* [2015]. The vTEC data are interpolated, by using natural neighbors, over a regular

grid covering latitudes from 20°S to 35°N and longitudes from 90°E to 135°E, with a spatial resolution of 0.5° in both latitude and longitude. vTEC values are provided for each point of the grid (lat, lon), for each day (dd), hour (HH) and every 10 min (Map(lat, lon, dd, HH, MM)). The interpolation technique has been selected according to *Cesaroni* [2015] and *Foster and Evans* [2008], who demonstrated that the natural neighbor interpolation is the best choice when regional TEC maps are considered. Mean TEC values  $\overline{\text{vTEC}}(\text{lat}, \text{lon}, \text{HH})$ , representing the quiet TEC conditions over the area of interest, are computed in each grid point reach hour, considering the above-defined quiet days of March 2015. Such background is subtracted from each vTEC value to evaluate the maps of the residuals  $\Delta\text{vTEC}(\text{lat}, \text{lon}, \text{dd}, \text{HH}, \text{MM})$  every 10 min for each of the days under investigation, as follows:

$$\Delta\text{vTEC}(\text{lat}, \text{lon}, \text{dd}, \text{HH}, \text{MM}) = \text{vTEC}(\text{lat}, \text{lon}, \text{dd}, \text{HH}, \text{MM}) - \overline{\text{vTEC}}(\text{lat}, \text{lon}, \text{HH}). \quad (3)$$

Hereafter,  $\Delta\text{TEC}$  represents the values of the residual of the vTEC.

### 2.1.3. Ionosonde Data

Concerning the ionosonde data, the critical frequency of the  $F_2$  layer ( $f_oF_2$ ) and the virtual height of the base of the  $F$  region ( $h'F$ ) are considered for Kupang and Sanya (Figure 1d).

The ionospheric station at Kupang is equipped with a Canadian Advanced Digital Ionosonde (CADI) [MacDougall *et al.*, 1995], and in March 2015 the sounding repetition rate and the sweeping frequency range were set to 15 min and from 1 MHz to 20 MHz, respectively. The ionospheric station at Sanya is equipped with a Digisonde [Bibl and Reinisch, 1978], and in March 2015 the sounding repetition rate and the sweeping frequency range were set to 7.5 min and from 1 MHz to 18 or 20 MHz, respectively. Data from Sanya are downloaded from the Global Ionospheric Radio Observatory web portal [Reinisch and Galkin, 2011].

From the same ionograms, also, the occurrences on the ionogram trace of the spread  $F$  phenomenon, for all the days of March 2015, between 10 and 25 March 2015, are analyzed.

Concerning the ionograms recorded at Kupang, a transformation of ionogram format is necessary from the MD4 one, which is the CADI native format, to the RDF format [Pezzopane, 2004], which is the format used in the Autoscala system [Pezzopane and Scotto, 2007, 2010; Cesaroni *et al.*, 2013] since the early stage of its development. Hence, all the ionograms recorded at Kupang are autoscaled by Autoscala, and afterward, the  $f_oF_2$  autoscaled values are validated using the Interpret software [Pezzopane, 2004]. The Interpret software is also used to validate the  $h'F$  characteristic, which is not given as output by Autoscala, from the ionograms recorded on 15, 16, 17, 18, 20, 21, 22, 23, and 24 March 2015.

Concerning the ionograms from Sanya, these are autoscaled by the Automatic Real-Time Ionogram Scaling with True-height system [Reinisch *et al.*, 2004; Galkin and Reinisch, 2008], and then the corresponding  $f_oF_2$  and  $h'F$  values are validated using the SAO explorer program developed by the University of Massachusetts, Lowell. By considering the quiet days defined above, the corresponding mean and standard deviation of the validated  $f_oF_2$  values have been calculated.

The ionograms recorded at Kupang and Sanya are also inspected to investigate the spread  $F$  phenomenon occurrence. Spread  $F$  signatures are manually categorized into two types: the range spread  $F$  (RSF) and the frequency spread  $F$  (FSF). RSF signatures present echo spreading occurring mainly along the height axis, and they are associated with plasma irregularities in the lower part of the  $F$  region. FSF signatures present echo spreading along the frequency axis close to the critical frequencies of the ordinary and extraordinary traces of the ionograms; hence, they are associated with irregularities nearby the  $F$  region peak.

### 2.1.4. Swarm Electron Density Data

The Swarm satellites are able to provide plasma measurements by means of the Langmuir Probes (LPs) located on the front of each satellite, i.e., in the direction pointing toward Earth. A LP determines local properties of the plasma, such as electron/ion temperature and density, by measuring the collected current due to electrons and ions. Data are provided at 2 Hz rate, and a quality flag is assigned to each sample. To our scope, the electron density  $N_e$  is the relevant parameter, and it has been used to support the ionospheric characterization of the St. Patrick's Day storm event. The electron density data used here are those of the so-called "Preliminary Level 1b Plasma Data Set" [Knudsen *et al.*, 2015]. The  $N_e$  data are not calibrated and, when compared with Constellation Observing System for Meteorology, Ionosphere and Climate radio occultation measures, the values provided have been found to underestimate the ionospheric electron density.

Depending on the geographical sector and time of the day, such difference ranges in the order of 8% to 15% [Pedatella *et al.*, 2015; Pignalberi *et al.*, 2016].  $N_e$  measured by Swarm at altitudes between 450 and 550 km has two characteristics: first, it is an in situ measurement and second, it is made in the topside ionosphere. Such characteristics must be taken into account when Swarm measurements are compared with vTEC data from GNSS, being the latter an integrated measurement of the electron density along the receiver-to-satellite raypath.

## 2.2. Magnetic Data

### 2.2.1. Ground-Based Magnetometers

As for the local observations of the geomagnetic field, data sets from four observatories have been considered. Two of these observatories are located in Vietnam and two in Indonesia, as shown in Figure 1c. The magnetometers are located in Phu Thuy, Da Lat, Pameungpeuk, and Watukosek, and their coordinates (latitude, longitude, and magnetic latitude) are reported in Table 1. All observatories are equipped with instruments compliant with the recommendations issued by International Association of Geomagnetism and Aeronomy, with a minimum set of one scalar and one vector magnetometer, whose baselines are determined by periodic absolute measurements. According to the geomagnetic coordinate system, the location of Da Lat (geomagnetic latitude 2.18°N) is the closest to the geomagnetic equator.

In the frame of geomagnetic studies at equatorial latitudes related to space weather, the *Dst* (disturbance storm time) index is commonly used to assign an empirical estimation of the severity of the Earth's magnetic condition during disturbed time [Mayaud, 1980; Rangarajan, 1989]. *Dst* provides an estimation of the variation of the *H* component at low latitudes. Along the lines of *Dst* index concept, we isolated the disturbance level at each observatory by subtracting the averaged nighttime values (01–04 hourly range of local time) of *H* from the time series of data, so as to obtain  $\Delta H$  values.  $\Delta H$  provides a self-normalization, which, in turn, allows for the comparison of magnitudes from different locations.

Besides the time evolution and periodicities of relevant known phenomena, the latitudinal and longitudinal spatial development of the disturbances have been investigated, leveraging on the geographic *L*-shaped displacement of the observatories. Specifically, couples of differentiated  $\Delta H$ ,  $\Delta(\Delta H)$ , have been used:

1. Da Lat minus Phu Thuy (DLT-PHU) and Da Lat minus Pameungpeuk (DLT-PMK): to identify the latitudinal dependence and the symmetry/asymmetry with respect to the geomagnetic equator;
2. Pameungpeuk minus Watukosek (PMK-WTK): to characterize the longitudinal variation;
3. Da Lat minus Watukosek (DLT-WTK): to provide extra information about two stations in two different longitudinal and latitudinal sectors.

### 2.2.2. Swarm Magnetometer Data

Aiming at maximizing the role of real physical data in place of static values from models, we derived the position of the magnetic equatorial line using the magnetic data set delivered by the Swarm mission. We used the data sets from all the three Swarm satellites, considering a time window of 3 months centered at the date of the St. Patrick's Day storm. At each satellite's flyby over the presumed position of the geomagnetic equator, the vertical component of the magnetic field inverts its sign. The positions where this occurs for different flybys of each satellite are averaged to obtain the estimated position of the magnetic equatorial line. Considering a travel speed of the Swarm satellites of about 7.6 km/s, we can conservatively consider a resolution of about 30 km in our determination of the magnetic equatorial line. The equatorial geomagnetic line, as determined by this procedure, is traced in Figure 1 together with isoclinic lines at  $\pm 15^\circ$  and  $\pm 20^\circ$ . Hereinafter, we refer to the dip equator and isoclinic lines as those measured with the Swarm mission data.

## 3. The Geospace During the St. Patrick's Day Storm Over SEA

The St. Patrick's Day storm was induced by sunspot numbered 2297 on 15 March 2015, from which a long-duration C9.1 flare and a partial, asymmetric halo coronal mass ejection are produced and resulted to be geoeffective, impacting the Earth on 17 March 2015 [Vanlommel, 2015]. In this section, we provide details of the storm development as measured by the regional monitoring infrastructures detailed in section 2.

The stacking plots of the horizontal components of the magnetic field for the four geomagnetic observatories are shown in Figure 2, arranged from the northernmost (Phu Thuy) to the easternmost (Watukosek)

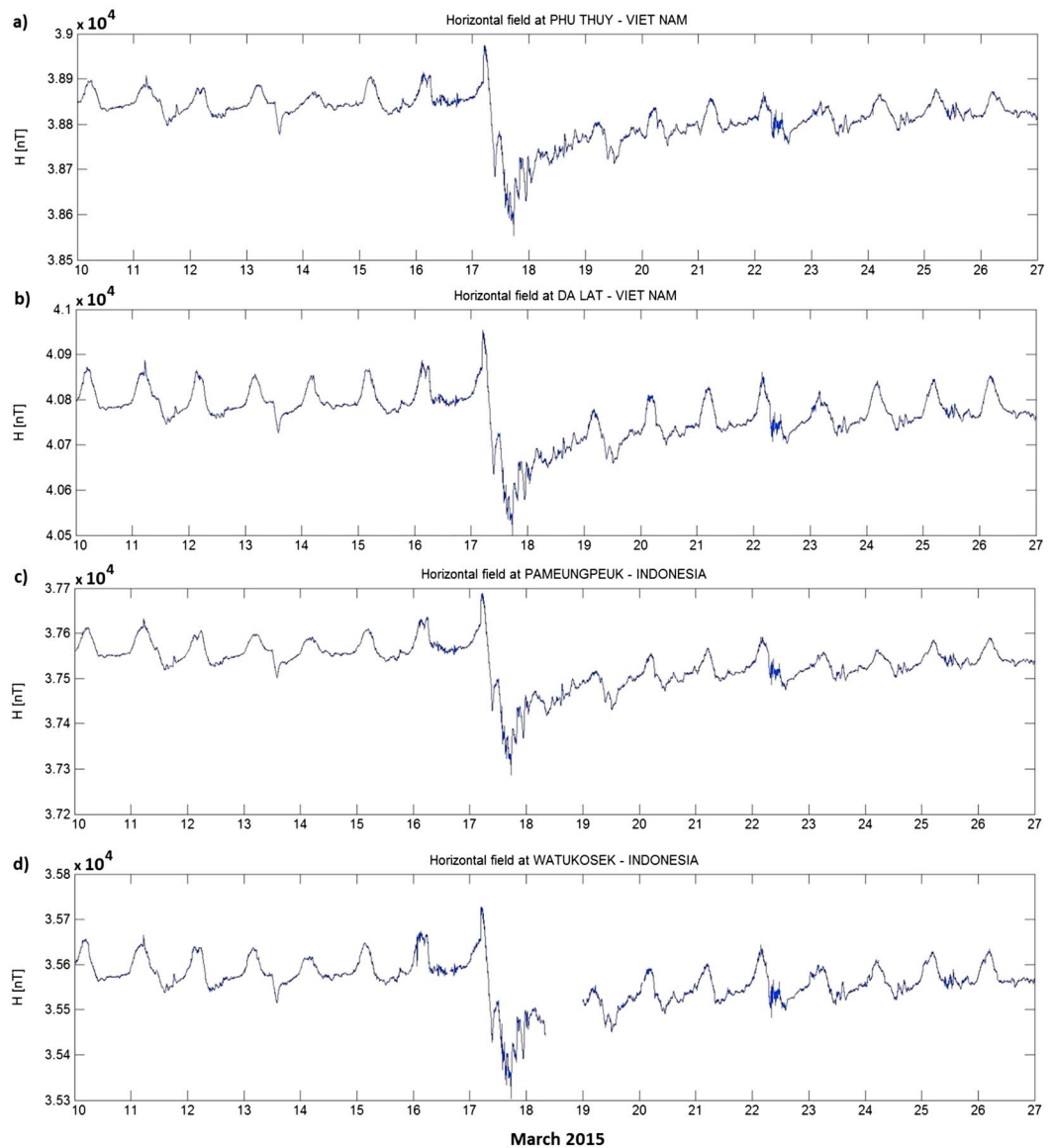


**Figure 2.** Horizontal component at the four geomagnetic observatories. The plots are arranged according decreasing latitude and increasing longitude (Phu Thuy, Da Lat, Pameungpeuk, and Watukosek).

observatory (reference in UT). Time profile of H in Da Lat (Figure 2b) shows the largest absolute magnitude, because of its proximity to the dip equator where horizontal values are indeed expected to be larger. A deeper analysis of the event is provided in Figure 3, where the local differences of the geomagnetic response, i.e., the time profiles of the horizontal deviation from undisturbed value  $\Delta H$  as defined in section 2.2.1, are shown. From this figure, some local features of the storm are highlighted:

1. the sudden storm commencement on 17 March 2015 at about 05 UT;
2. the substorm signature roughly between 12 and 14 UT on the same day confirms the observations on  $\Delta H$  plots by *Tulasi Ram et al.* [2016] in the equatorial zone of the Pacific sector and for the same storm time. Simultaneous increase (or decrease) in  $\Delta H$ , named as positive (or negative) bay, is an indication of the enhanced eastward (or westward) electric field perturbations associated with the onset of substorms. This in turn gives important contributions to the settlement of the local perturbed ionospheric scenario and its evolution [*Sastri et al., 2003; Huang, 2009, 2012*].
3. the main phase between 05 and 23 UT on the same day;

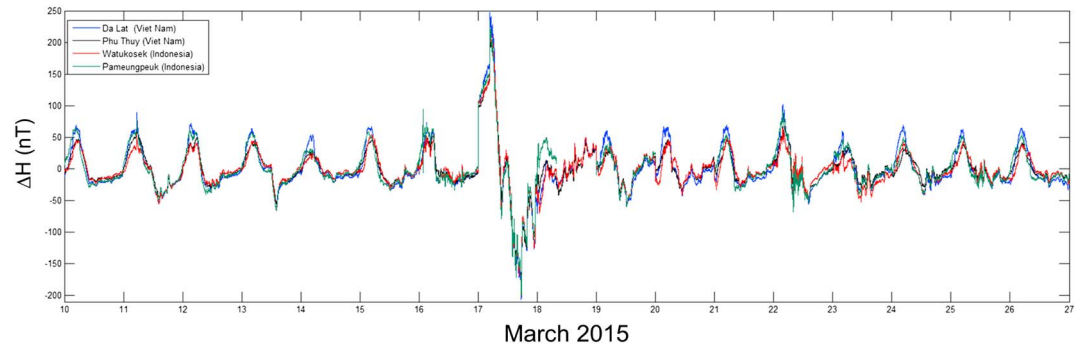


**Figure 3.** Time profile of  $\Delta H$  values for Da Lat (blue), Phu Thuy (black), Watukosek (red), and Pameungpeuk (green) magnetic observatories.

4. the recovery phase characterized by several significant magnetic variation signatures, as discussed below. The signatures of the substorm events present slight differences among the considered stations. The most noticeable is the one on 18 March at Pameungpeuk (green line in Figure 3). For this particular magnetometer, the rise of  $\Delta H$  is faster than in the other sites, even if a data gap after 18 March does not allow further characterizations of this local features. In each observatory, the recovery phase is found to be noticeably long (more than 10 days).

To evaluate both time and spatial evolutions at latitudinal and longitudinal extension, in Figure 4 we stacked the four couples of  $\Delta(\Delta H)$ , as mentioned in the bullet points in section 2.2.1. To be specific, couples are Da Lat minus Phu Thuy (light blue line), Da Lat minus Pameungpeuk (blue line), Da Lat minus Watukosek (red line), and Pameungpeuk minus Watukosek (black line). The most evident arising features are the large differentiated values of the traces regarding the couples DLT-PHU (reaching  $-73$  nT) and DLT-PMK (reaching  $-29$  nT), and the minimum occurred at the change of date in UT (17–18 March). This is the most singular event of the whole analyzed period of time (17 days) when traces of couples DLT-WTK and PMK-WTK are out of phase with respect to the above two traces. In other cases, some interesting phase delays or anticipations and other peculiarities can be recognized among the different curves, including the unique opposition of phase in the time series for the couple PMK-WTK (black line in Figure 4), occurred on first part of 24 March, and a general increase of the dynamic level for this couple, which takes place since 20 March.

From the ionospheric point of view, the behavior of the electron density variation during the storm development is reported in Figure 5. Figure 5a of this figure shows the latitudinal dependence of the vTEC measured by the IGS receivers from 15 to 25 March 2015. Figure 5b reports  $N_e$  measured in situ by the three Swarm satellites in the same latitudinal range of the vTEC. These plots are produced considering both vTEC and electron density data in the longitudinal range between  $90^\circ\text{E}$  and  $135^\circ\text{E}$ . Data distribution follows the geometry and availability of the IGS TEC and Swarm data. In particular, some gaps in the RINEX data resulted in a lack of coverage in Figure 5a in the range between  $0^\circ\text{N}$  and  $5^\circ\text{N}$  starting from 21 March. The gaps in Figure 5b are due to the different flybys of the Swarm satellites, which do not allow a full coverage at all local times. Dissimilarities between Figures 5a and 5b are likely due to the fact that  $F$  layer and topside ionosphere may not respond in the same way to a solar event [see, e.g., Yizengaw *et al.*, 2006; Astafyeva *et al.*, 2015a]. By

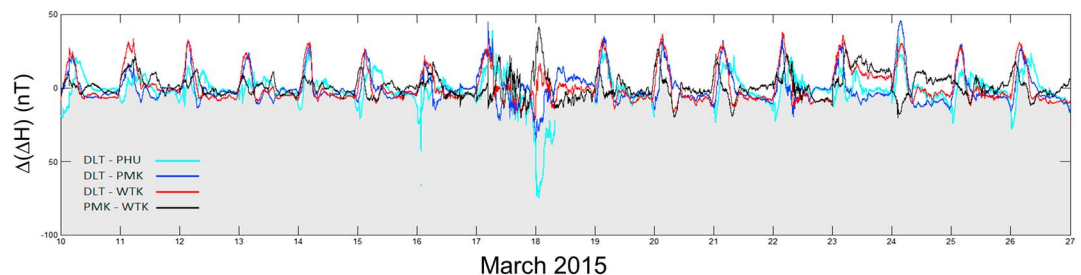


**Figure 4.** Differentiated  $\Delta H$  for the couples DLT-PHU (light blue line), DLT-PMK (blue line), DLT-WTK (red line), and PMK-WTK (black line).

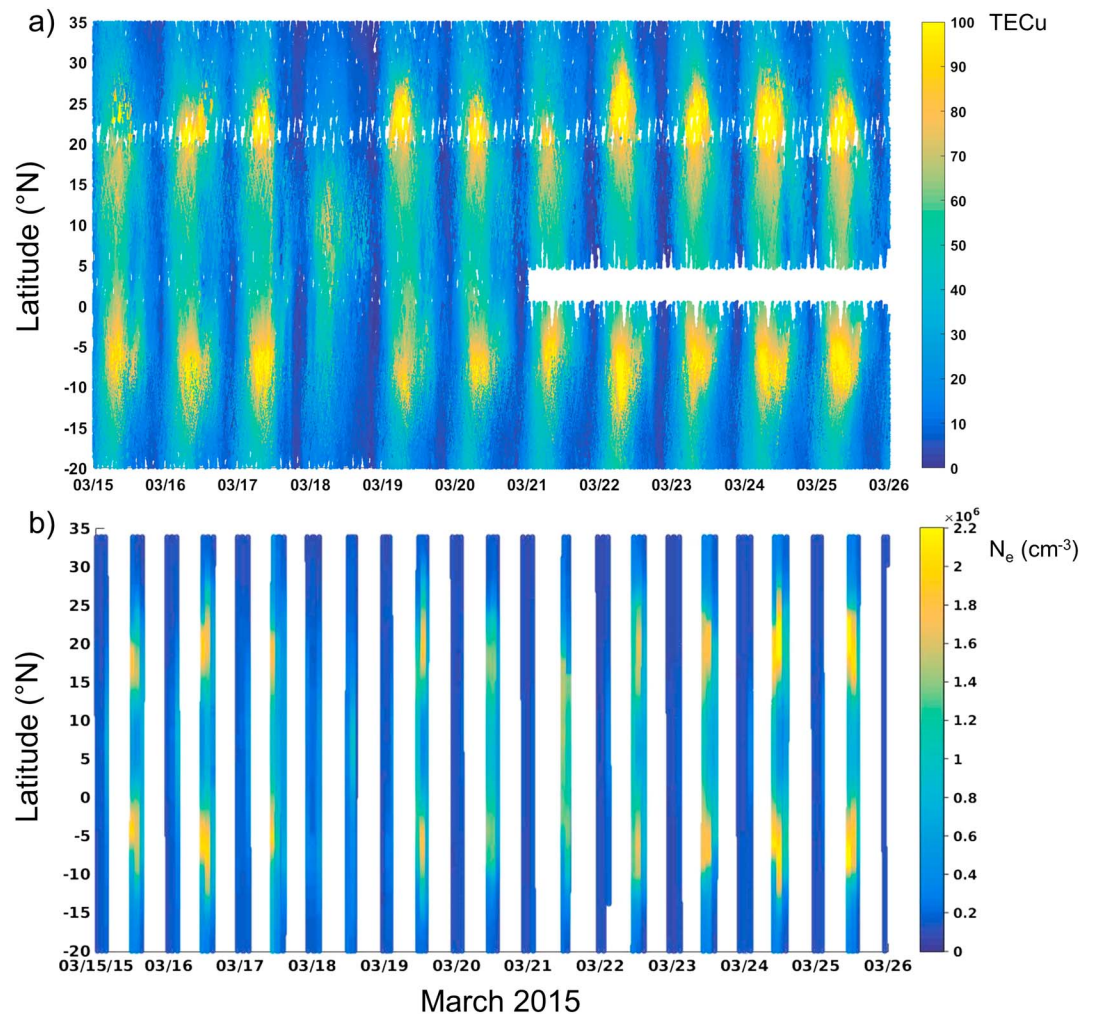


**Figure 5.** (a) Total electron content and (b) in situ electron density as measured by Swarm A, B, and C as a function of the geographic latitude from 15 to 26 March 2015.

capturing differences and similarities between the two characterizations of the electron density, it is possible to derive some interesting features. To be specific, both the observations reveal how the typical configuration of two crests of the EIA is completely lost on 18 March, i.e., at the beginning of the recovery phase. By looking at vTEC data only (Figure 5a), it is interesting to note how the two-crest configuration is always present, except on 18 March. Some asymmetries of the crests are also visible from vTEC data: except for 15 March, northern crest during the storm are characterized, when present, by larger values of vTEC. Then again, excluding the already mentioned lack of the crests on 18 March, the following features arise when analyzing Swarm data (Figure 5b):

1. crests disappear at earlier time on 17 March;
2. signature of the crests is lost on 21 March;
3. signature of the crests is weak between 20 and 23 March;
4. crests start reappearing with a clear signature from 24 March onwards.

In summary, comparing vTEC and Swarm data, it is interesting to note that from 20 to 24 March, the crests signature visible in vTEC are not clearly identified with in situ data, meaning that the  $E \times B$  is not strong enough to make crests reaching the Swarm altitudes.

To exemplify the inhibition of the crests on 18 March, Figure 6 shows the electron density measured by Swarm satellite A between 19:45 and 19:56 LT during 15 March 2015 (Figure 6a) and between 19:29 and 19:40 LT during 18 March 2015 (Figure 6b). Thus, both plots refer to a Swarm track passing in the SEA region

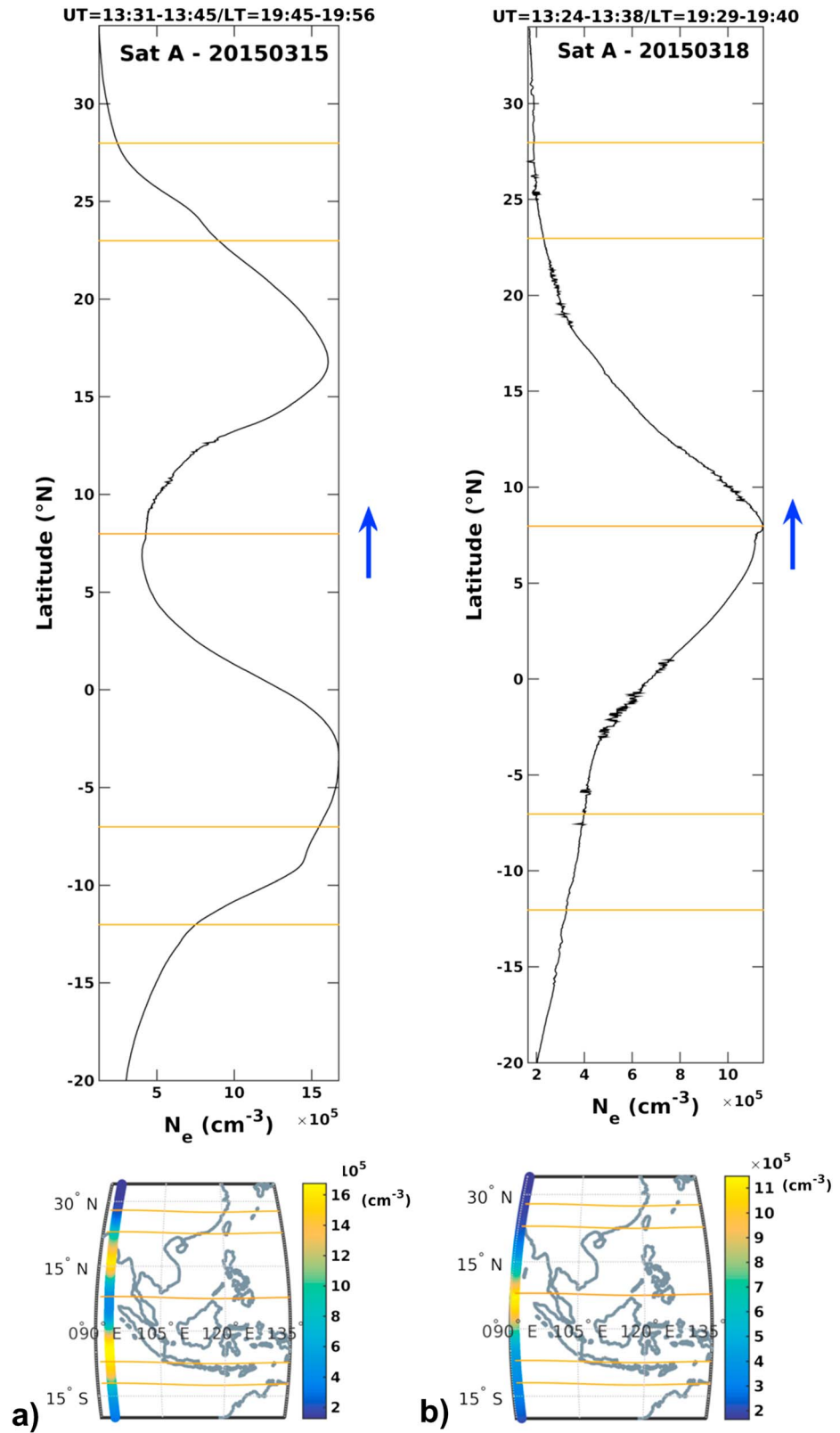


**Figure 6.** Electron density measured by Alpha Swarm satellite (a) between 19:45 and 19:56 LT during 15 March 2015 and (b) between 19:29 and 19:40 LT during 18 March 2015. The blue arrows indicate the flight direction of the satellite. The orange lines represent the position of the dip equator in March 2015 as measured by the Swarm constellation of satellites and the isoclinic lines at  $\pm 15^{\circ}$  and  $\pm 20^{\circ}$ .

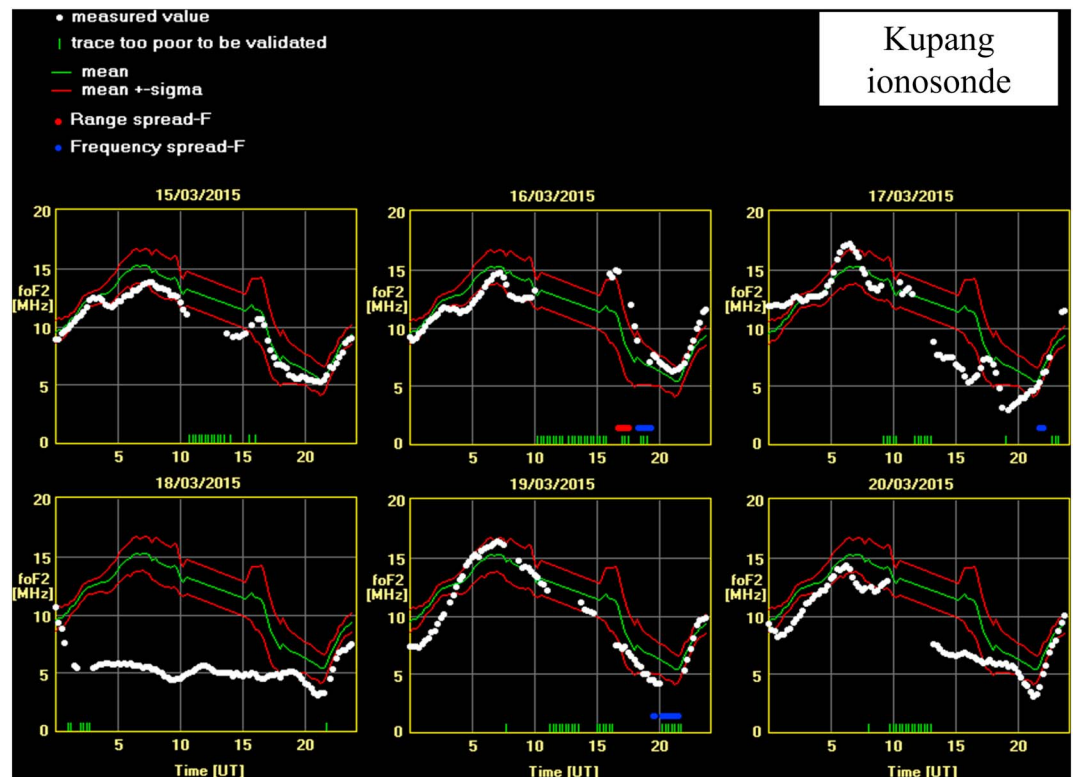


**Figure 7.**  $f_oF_2$  as measured (white dots) at Kupang from 15 to 20 March 2015, together with the corresponding mean (green curve) and standard deviation (red curves above and below the mean curve represent the mean  $\pm$  the standard deviation, respectively), calculated according to the 15 quietest days of March 2015. The red and blue dots at the bottom of each plot highlight the presence of range spread  $F$  and frequency spread  $F$ , respectively. The green vertical short lines at the bottom of each plot mean that the ionogram is recorded but the trace is too poor to validate a reliable value of  $f_oF_2$ .

at about 90°E in the local postsunset hours. In the figure, the blue arrows indicate the flight direction of the satellite, while the orange lines represent the position of the dip equator and of the isoclinic lines at  $\pm 15^\circ$  and  $\pm 20^\circ$ . Figure 6a represents the quiet ionospheric conditions, as 15 March is one of the days assumed to be quiet in our study. In fact, the two-crest configuration is clearly present on 15 March, with the two maxima of the electron density of about  $1.6 \times 10^6$  el/cm<sup>3</sup>, symmetric with respect to the dip equator. Such configuration is completely lost on 18 March (Figure 6b), as a single peak of about  $1.1 \times 10^6$  el/cm<sup>3</sup> in correspondence with the dip equator is present. Furthermore, on the 18 March track, fluctuations of the electron density are present, especially around 20°N, 10°N and between 1°S and 5°S, indicating spatial gradients of the electron density along the track. Such fluctuations are absent on 15 March, except between 10°N and 13°N, but less intense than those recorded on 18 March, indicating a more regular behavior of the ionosphere during 15 March than during 18 March, as expected.

Our observations are also reinforced by what was found by Carter *et al.* [2016], who reported the weakening of the interplanetary electric field at ~00 UT on 18 March (corresponding to the postmidnight sector in SEA), which led to the weakening of the RTI growth rate. In the following days, Carter *et al.* [2016] reported also the absence of RTI formation.

From the ionosonde point of view, to study the spatial extent of the ionospheric plasma behavior during the storm, Figures 7 and 8 show the  $f_oF_2$  values as measured at Kupang and Sanya, respectively, from 15 to 20 March 2015, together with the corresponding mean value and standard deviation calculated on the basis of quiet days. The red and blue dots in each plot highlight the presence of RSF and FSF, respectively. The green vertical short lines at the bottom of each plot mean that the ionogram is recorded but the trace is too poor to validate a reliable value of  $f_oF_2$ . From such figures, both ionosondes show evidence of a negative ionospheric storm, as  $f_oF_2$  is well below the mean value for most of 18 March 2015. By comparing the response to the storm depicted by the two ionosondes, we remind the reader that the two ionosondes are

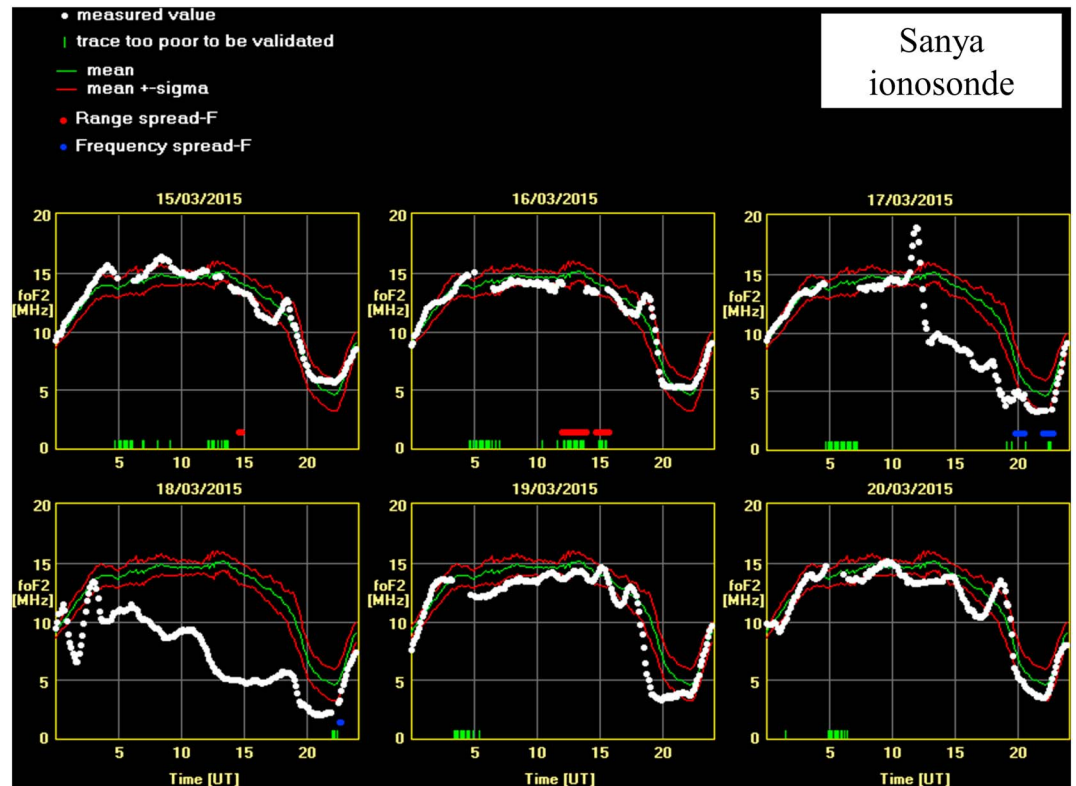


**Figure 8.** Same as in Figure 7 but for the ionosonde in Sanya.

below the northern and southern crests of the EIA but in two different longitudinal sectors. Both at Kupang and Sanya, the  $f_oF_2$  values show that the onset is trailed by an impulsive positive ionospheric storm occurring at Kupang at about 06 UT (14 LT) and, in a more pronounced manner, at Sanya at about 11 UT (18 LT). Then, through the second half of 17 March and the whole day of 18 March,  $f_oF_2$  is significantly smaller than the lower boundary limit defined by the mean minus the standard deviation. Negative storms like this at middle and low latitudes are caused by changes of the neutral components in the ionosphere [Buonsanto, 1999]. Specifically, at  $F$  layer heights this negative phase is likely due to the reduction of the ratio between atomic oxygen and molecular nitrogen that meaningfully increase the rate of ion loss [Prölss, 1995]. This composition anomaly moves equatorward from the auroral latitudes with the disturbance meridional neutral wind of the storm. According to the different time of the year, it can move more or less far, with negative storms extending to lower latitudes in the summer hemisphere. The fact that the negative phase is more pronounced at Kupang than at Sanya might be due to this issue, being Kupang in the summer hemisphere while Sanya in the winter hemisphere. Also, Nayak *et al.* [2016] reported such hemispherical asymmetry but in the American and European sectors, suggesting that such asymmetry is a nonlocal effect related to the neutral wind circulation and to the equinoctial conditions [Fuller-Rowell *et al.*, 1996; Goncharenko *et al.*, 2007].

Figure 9 shows the  $h'F$  trend as measured at Kupang (Figure 9a) and Sanya (Figure 9b), from 16 to 18 March 2015. Also in this figure, the green vertical short lines at the bottom of each plot denote that the ionogram is recorded but the trace is too poor to validate a reliable value of  $h'F$ . The most striking feature appearing in Figure 9 is the double peak characterizing the UT afternoon of 17 March. The first peak appears at the same time in both ionosondes (16 UT), while the second peak appears earlier at Kupang (20 UT–04 LT) than in Sanya (22 UT–05 LT), with corresponding amplitudes well past 400 km of altitude each. This is likely caused by the intense substorm activity characterizing the main phase of the storm in this time window. In fact, during a magnetic substorm a significant amount of energy is injected into the polar atmosphere. This sudden energy addition gives rise to a so-called traveling atmospheric disturbance (TAD) that can cause an uplifting of the  $F$  layer, which usually increases the electron density. This mechanism is however applicable only to the daytime ionosphere, when the ionization production is ongoing [Prölss, 1995]. In this case, the

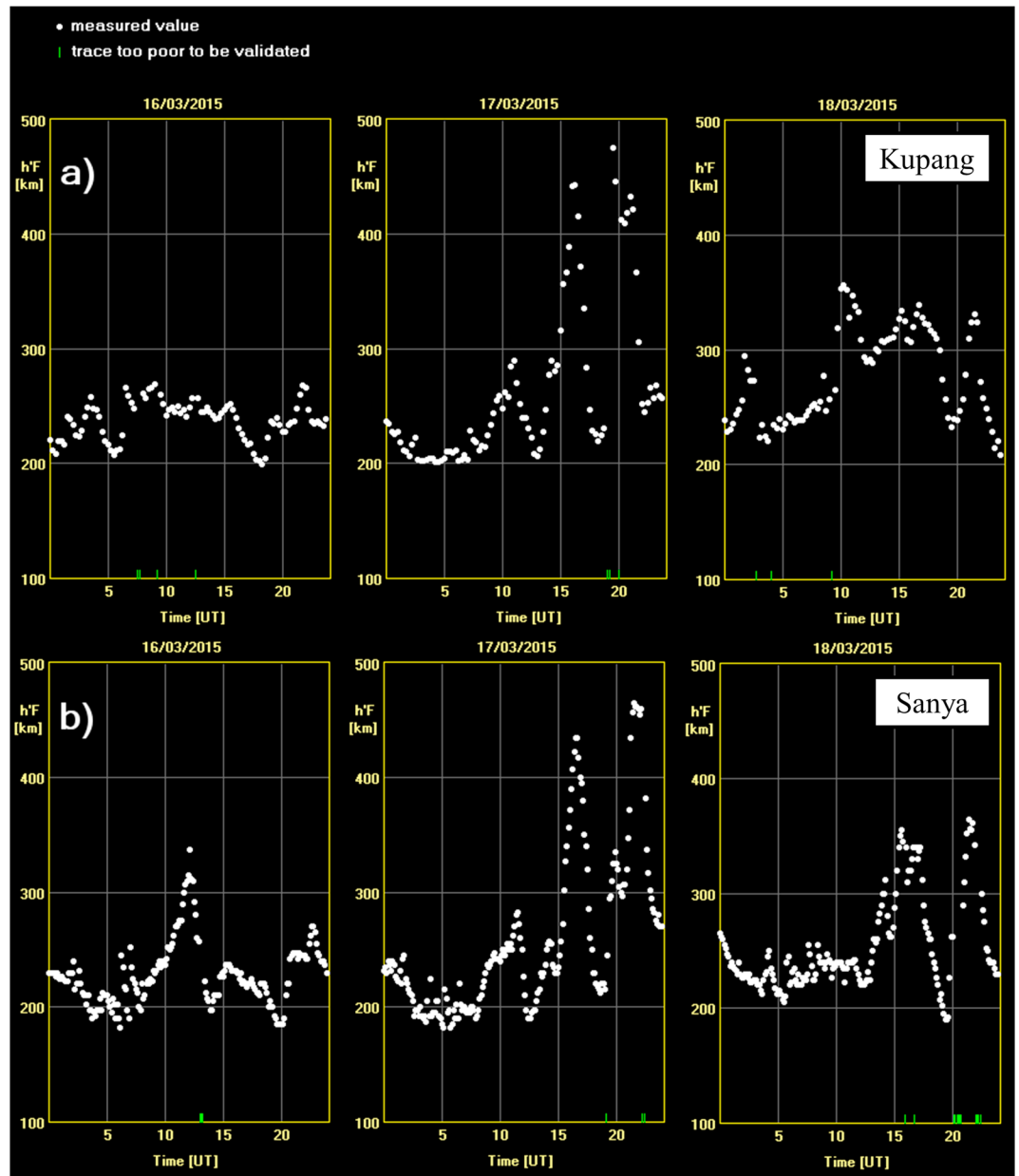


**Figure 9.**  $h'F$  as measured at (a) Kupang and (b) Sanya from 16 to 18 March 2015. The green vertical short lines at the bottom of each plot mean that the ionogram is recorded but the trace is too poor to validate a reliable value of  $h'F$ .

double uplift of the layer, likely associated to TADs, which are independent of the local time, occurs in the nighttime sector, and then it is not accompanied by a positive ionospheric phase.

#### 4. Results and Discussion

Besides depicting the main observational features of the St. Patrick's Day storm, in this section we show results of the investigations conducted by integrating the measurements provided by the regional networks. To be specific, particular emphasis is given to the ionospheric scintillation (presence/inhibition) and its correspondence to geospace variations.

In order to give a climatological picture of the scintillation activity in the studied period, the GBSC technique has been applied to provide scintillation occurrence over SEA. Figure 10 illustrates the GBSC maps of occurrence of  $S_4$  above 0.1 (Figures 10a and 10b) and 0.25 (Figures 10c and 10d) as a function of latitude

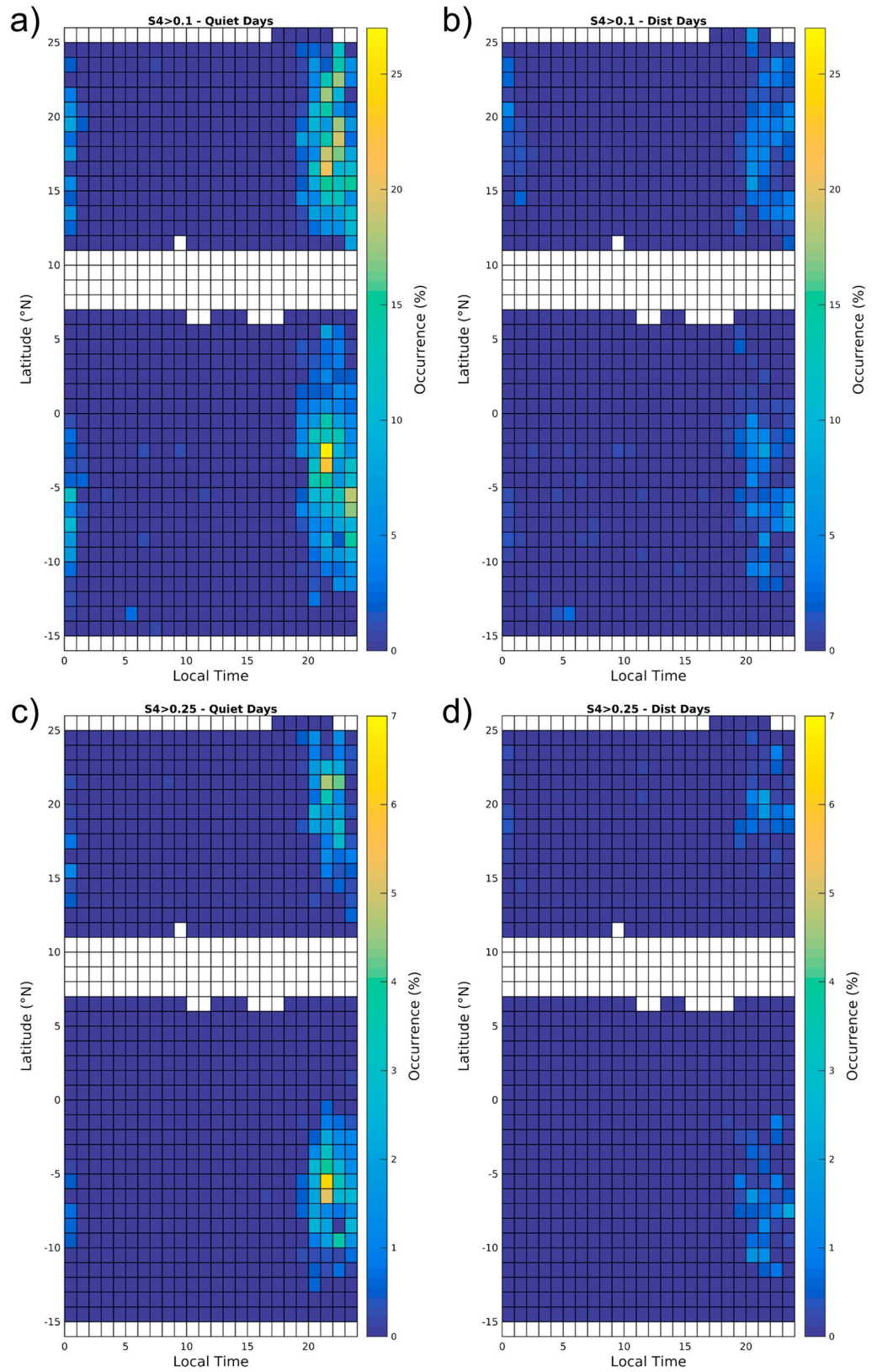


**Figure 10.** GBSC maps of occurrence of  $S_4$  above (top) 0.1 and (bottom) 0.25 as a function of latitude and local time for (left) quiet and (right) disturbed days of March 2015. The ratio between quiet and disturbed days in March is 48.4%.

and LT for quiet (Figures 10a and 10c) and disturbed (Figures 10b and 10d) days of March 2015. Such thresholds are commonly used to be representative of the weak to strong scintillation (threshold 0.1) and of the moderate to strong scintillation (threshold 0.25) conditions [see, e.g., Spogli *et al.*, 2009; Prikryl *et al.*, 2015]. Maps have been obtained by merging the observations made by all the satellites in view by each scintillation receiver (Figure 1a); adopted bin size is  $1^\circ$  latitude  $\times$  1 h. In all the four maps, the enhancement of the scintillation occurrence maximizes between 19 and 01 LT, the local postsunset hours, and in correspondence to the position of the EIA crests. A meaningful decrease of the scintillation occurrence is recorded during disturbed days (Figures 10b and 10d), indicating that the inhibition of the scintillation phenomena is the predominant feature in the SEA sector during the considered disturbed days. The partial inhibition during disturbed days is a signature of the complexity behind the enhancement (suppression) of the  $F$  layer uplift, prompting (impeding) the ionospheric irregularity formation [Aarons, 1991; Dabas *et al.*, 2003; de Rezende *et al.*, 2007; Ngwira *et al.*, 2013].

It is also interesting to notice the difference between the pattern of scintillation occurrence in correspondence to the northern and southern crests of EIA. Specifically, the southern crest is statistically characterized by a larger occurrence, possibly meaning that the variability of the electron density gradients leading to amplitude scintillation is statistically larger in the southern crest of the EIA [see, e.g., Cesaroni *et al.*, 2015]. Although occurrence is normalized to the number of observations, a second-order contribution derived by the different coverage under the two crests cannot be excluded.

Then, to resolve the relationship between the scintillation patterns and the variability of the ionospheric plasma in the different storm phases, Figure 11 shows the longitudinal mean of  $\Delta$ TEC values (see equation (3)), derived by IGS RINEX data. In each plot of this figure, the black dots represent the IPP latitude and time in which  $S_4$  values greater than 0.1 have been recorded. To relate  $\Delta$ TEC and scintillation to the different phases of the St. Patrick's Day storm evolution, the  $Dst$  index has been also superimposed in the figure (purple line). The black dashed lines represent the magnetic equator (tick line) and the isoclinic lines corresponding to  $\pm 15^\circ$  and  $\pm 20^\circ$  magnetic latitude (thin lines). The three plots correspond to different longitudinal sectors. In particular, Figure 11a shows the mean  $\Delta$ TEC and  $S_4$  values acquired considering all the longitudinal sectors, i.e., from  $90^\circ\text{E}$  to  $135^\circ\text{E}$ , while Figures 11b and 11c include the longitudinal mean  $\Delta$ TEC and  $S_4$  values corresponding to longitudes between  $108^\circ\text{E}$  and  $111^\circ\text{E}$  and between  $122^\circ\text{E}$  and  $125^\circ\text{E}$ , respectively. Hereafter, we refer to the range of  $108^\circ\text{E}$  to  $111^\circ\text{E}$  as the western sector and  $122^\circ\text{E}$  to  $125^\circ\text{E}$  as the eastern sector. Figure 11a shows that the  $\Delta$ TEC behavior is perturbed mostly during the recovery phase of the storm. In particular, during 18 March (i.e., at the beginning of the recovery phase), a huge depletion of  $\Delta$ TEC reaching  $-80$  total electron content unit,  $1 \text{ TECU} = 10^{16} \text{ el m}^{-2}$ , represented by the deep blue area (corresponding to about  $-80 \text{ TECU}$ ), can be noticed. A similar depletion is reported also on topside TEC data in Figure 4 of Zhong *et al.* [2016]. The  $\Delta$ TEC values remain lower than those of quiet days until 24 March, when  $v$ TEC reaches values greater than the background both in the crests and the trough region (red area in Figure 11a). During the main phase of the storm, mean  $\Delta$ TEC is mostly negative, except from 12 to 13 UT, when positive values of the mean  $\Delta$ TEC have been registered, likely related to the simultaneous substorm input (visible in the  $Dst$  curve superimposed in purple color in the plots of Figure 11). The observed inhibition of scintillation happens during the main and recovery phases of the storm (from 17 to 24 March).

According to the Aarons criteria [Aarons, 1991, Figure 1], more suitable conditions for scintillation inhibition stand if the maximum  $|Dst|$  is reached between 10 and 16 LT. Less suitable, but changing the scintillation patterns after the sunset, is the case 00–06 LT, while the case 18–22 LT does not change meaningfully the expected formation of scintillation-driving irregularities. In the case of the Saint Patrick's Day storm, the minimum  $|Dst|$  occurred at 23 UT, corresponding to local times between 06 and 08, depending on the longitudinal sectors. Thus, in the considered region, according to the Aarons criteria, little changes are expected in westernmost sectors, while no a priori information can be provided for the other sectors. In any case, scintillation inhibition is clearly present during the main (17 March) and beginning of the recovery (18 March) phases of the storm.

In Figure 11, most of the scintillation occurs when mean  $\Delta$ TEC is positive, while it is inhibited when mean  $\Delta$ TEC is negative. Some differences on the  $v$ TEC behavior during the recovery phase of the storm can be highlighted when comparing western and eastern sectors, in Figures 11b and 11c, respectively. Such differences

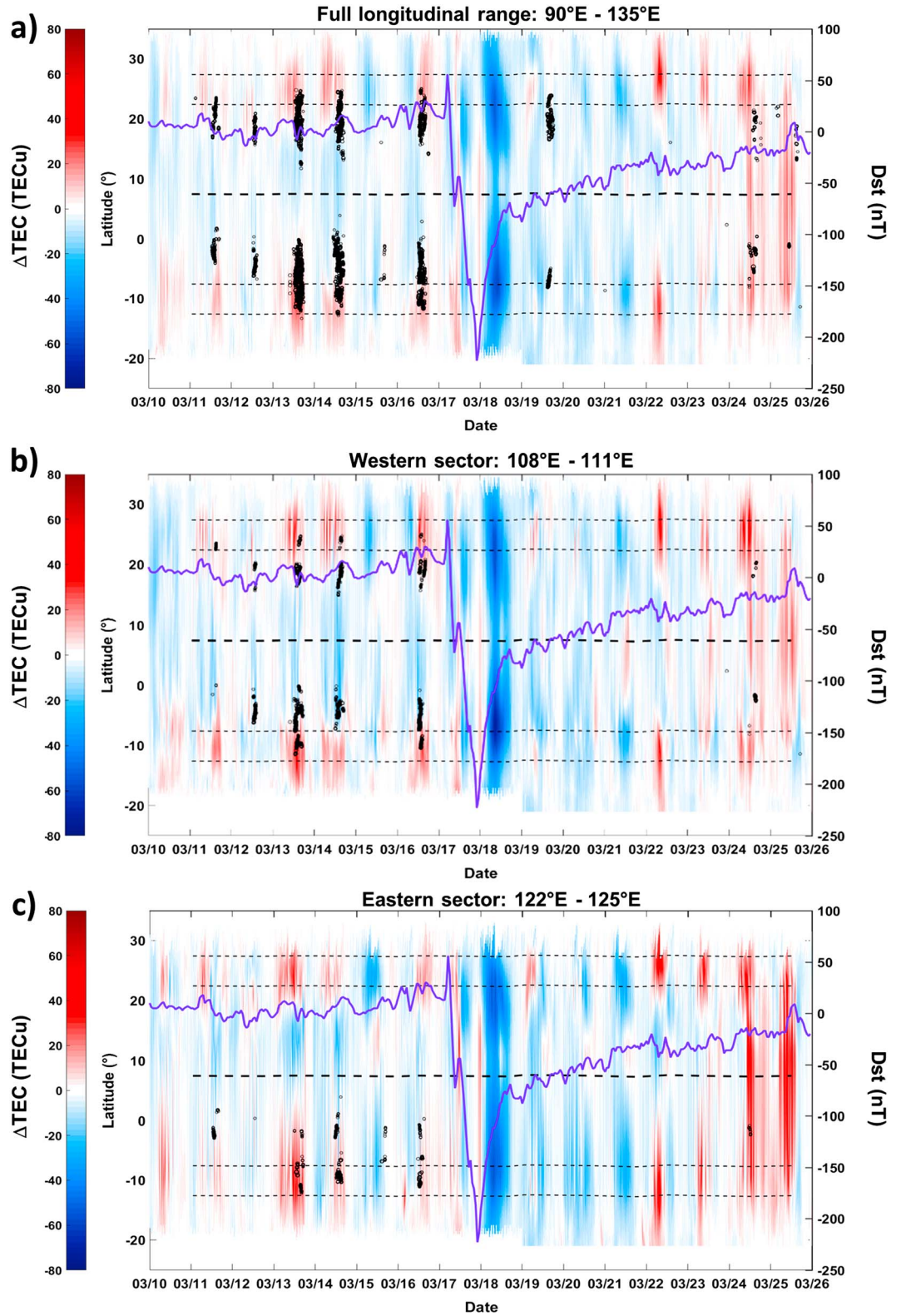


**Figure 11.** Mean value of  $\Delta\text{TEC}$  (a) for all longitudinal sectors and (b) for the longitude between 108°E and 111°E and between 122°E and 125°E as a function of latitude from 15 to 26 March 2016. Dimension of the black dots is proportional to  $S_4$  and is shown only if  $S_4 > 0.1$ . The purple line is the  $Dst$  index. The black dashed lines represent the position of the dip equator as measured by the Swarm constellation of satellites and the isoclinic lines at  $\pm 15^\circ$  and  $\pm 20^\circ$ .

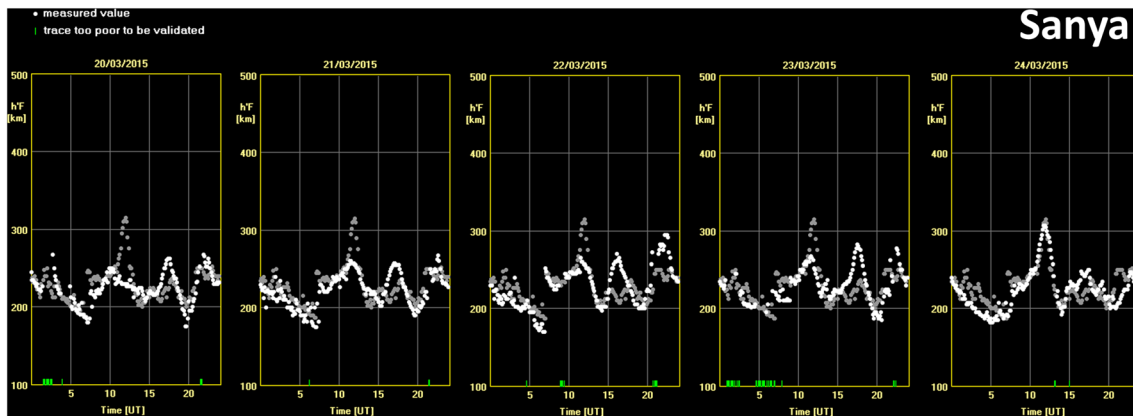


**Figure 12.**  $h'F$  as measured at Sanya from 20 to 24 March 2015. The green vertical short lines at the bottom of each plot mean that the ionogram is recorded but the trace is too poor to validate a reliable value of  $h'F$ . The same gray curve in each of the plots represents the  $h'F$  values measured at Sanya on 15 March 2015 and here considered as the quiet reference day (analogously to *Nava et al.* [2016]).

are more evident in the trough region. In fact, the vTEC recovery to quiet values started on 21 March in the western sector and on 22 March in the eastern one. In the crests, some differences can be caught as well: eastern sector seems to show larger mean  $\Delta\text{TEC}$  than the western one on both northern and southern crests, starting from 22 March.

Further information about the mechanisms leading to the scintillation inhibition and triggering can be provided by comparing Figure 11a with the vTEC and  $N_e$  information provided by Figure 5, in which all longitudinal sectors from  $90^\circ$  to  $135^\circ$  are considered. As already pointed out in section 3, the crests disappear earlier on 17 March, as visible in the UT afternoon Swarm tracks in Figure 5b. In correspondence, scintillation inhibition has been found, as it is visible in Figure 11a. The crest disappearance at earlier time in Swarm data is also in correspondence to the substorm signature at about 13 UT, related to 19/21 LT depending on the longitudinal sector. Such results indicate that the ionospheric  $F$  layer is pushed to lower altitudes with respect to the Swarm heights but with an increased electron density visible as positive  $\Delta\text{TEC}$  values in Figure 11a. This is the result of the  $F$  layer shrinking, already reported by Figure 11 of *Nava et al.* [2016].

On 19 March, the scintillation at postsunset reappears, in particular under the northern crest, where a slightly positive deviation from the quiet  $\Delta\text{TEC}$  behavior is present (Figure 11a). The scintillation near the southern crest on 19 March is in correspondence to very small values of  $\Delta\text{TEC}$ , i.e., very small negative deviations from the quiet behavior (Figure 11a). The crests are well depicted by vTEC and  $N_e$  data on 19 March, with a larger intensity of the northern crest, more evident in vTEC data (Figure 5).

Despite the fact that crests are well depicted by vTEC data on 20 and 21 March (Figure 5a), they are not visible in the Swarm data (Figure 5b) and, in correspondence, scintillation is inhibited. This reinforces the idea that the altitudes reached by the  $F_2$  layer are the main cause behind the inhibition or triggering of irregularity formation in the plasma cascade, induced by the changes in the upward density gradient generated by the westward electric field near sunset [*Ngwira et al.*, 2013].

Starting from 22 March, crests reappear on Swarm data (Figure 5b), but scintillation starts occurring again only on 24 March (Figure 11a). This could mean that the  $F_2$  layer heights required to produce the plasma cascade under the gravity are above or close to the Swarm altitudes on 24 March and well below from 20 to 23 March. This is confirmed by Figure 12, which reports that at 12 UT from 20 to 23 March the  $h'F$  values recorded in Sanya, and manually validated, are by far lower than the quiet regular ones (the 15 March is considered as the quiet reference day, analogously to *Nava et al.* [2016]), while the 24 March at 12 UT the  $h'F$  fully recovers to its normal values.

This would mean that between 20 and 23 March the irregularities embedded in plasma bubbles do not reach scales below the Fresnel's one; i.e., they are not effective in producing scintillation (Figure 11a).

The pattern of the daily postsunset scintillation is restored starting from 24 March, even with a smaller intensity with respect to the quiet times (Figure 11a).

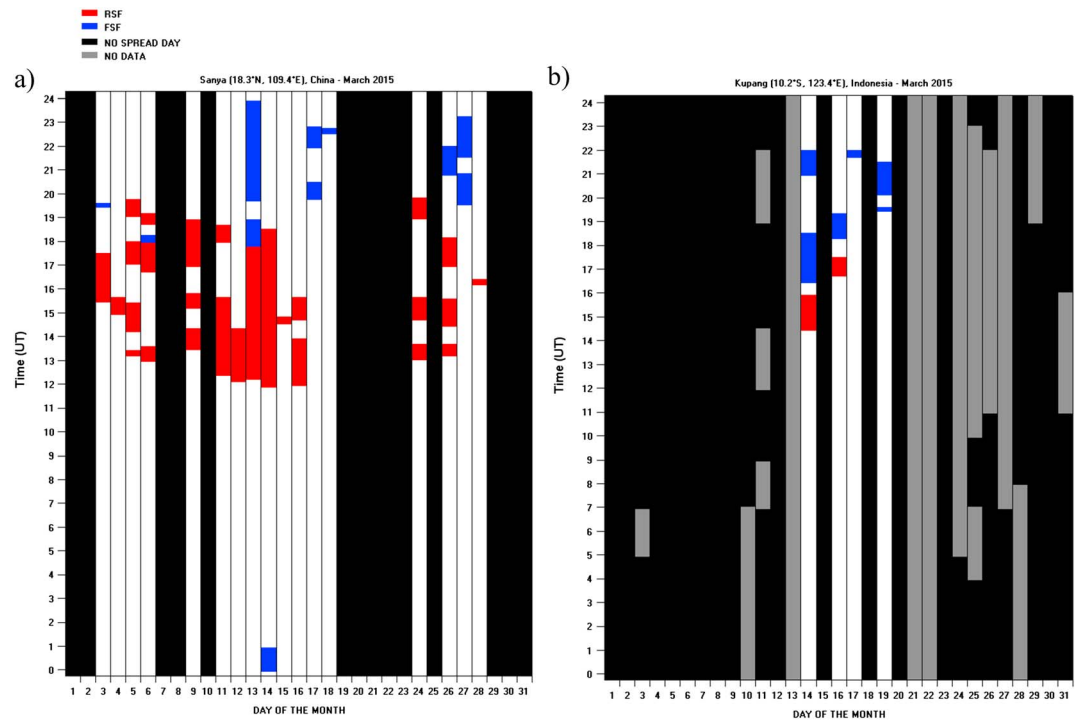


**Figure 13.** Range spread *F* (red) and frequency spread *F* (blue) occurrence at (a) Sanya, China and (b) Kupang, Indonesia for March 2015. Gray means data unavailability. Black highlights no spread *F* days.

Such observations are in agreement with the modeled RTI growth rate and amplitude scintillation observations in Bangkok (13.75°N, 100.48°E) reported in Figure 2l of Carter *et al.* [2016].

To provide further insights about the ionospheric irregularities occurred during the St. Patrick's Day storm and their correspondence to scintillations, the ionograms recorded at Kupang and Sanya are sifted through to identify spread *F* occurrence. As mentioned earlier in the text, RSF identifies irregularities in the lower part of the *F* region, while FSF identifies irregularities nearby the *F* region peak. As reported in the climatological work by Alfonsi *et al.* [2013], different types of spread *F* correlate (or anticorrelate) in a different way with scintillation occurrence, and thus, it is worth providing a picture of such correspondence. The rectangles in blue color in Figure 13 depict the occurrence of FSF, while the red color identifies the RSF occurrence, both as a function of the day of March 2015 and of the universal time (local time = universal time + 7/8 h). The gray color indicates the data unavailability and the black color days for which ESF is not recorded. Figure 13a refers to the ionosonde in Sanya, which is representative of conditions below the northern crest of the EIA at about 109°E, while Figure 13b refers to the ionosonde in Kupang, which is representative of the southern crest of the EIA at about 123°E. It is interesting to notice how the occurrence in Sanya of both RSF and FSF is larger than in Kupang. In particular, RSF occurrence is concentrated in the local postsunset hours, while FSF occurs mainly in the local night/early morning. During the main phase of the storm (17 March), the RSF is completely suppressed in both ionosondes and only FSF has been recorded after 19 UT. Some lack of ionograms limits the possibility to draw a detailed picture of the recovery phase in Kupang. However, in Kupang both RSF and FSF are suppressed on 18 March, i.e., at the beginning of the recovery phase. Again in Kupang, only on 23 and between 28 and 31 March the absence of both RSF and FSF has been recorded. At Sanya, FSF is present between 22 and 23 UT (05 and 06 LT) on 18 March and the spread *F* formation is inhibited for the following 5 days, up to 23 March. On 24 March, the RSF reappears and, after a new complete inhibition on 25, RSF and FSF are again present between 26 and 28 March. Hence, although noncontinuous as that characterizing the L-band scintillations, inhibition appears as a significant feature also in the HF frequencies.

In the equatorial ionosphere, ESF is confirmed to be a nighttime summer phenomenon [see, e.g., Alfonsi *et al.*, 2013]. Figure 14 details the scintillation occurrence at Hue (Figure 14a) and Kupang (Figure 14b). Such receivers have been chosen for their proximity to the ionosondes. In Kupang, the ionosonde and the receiver

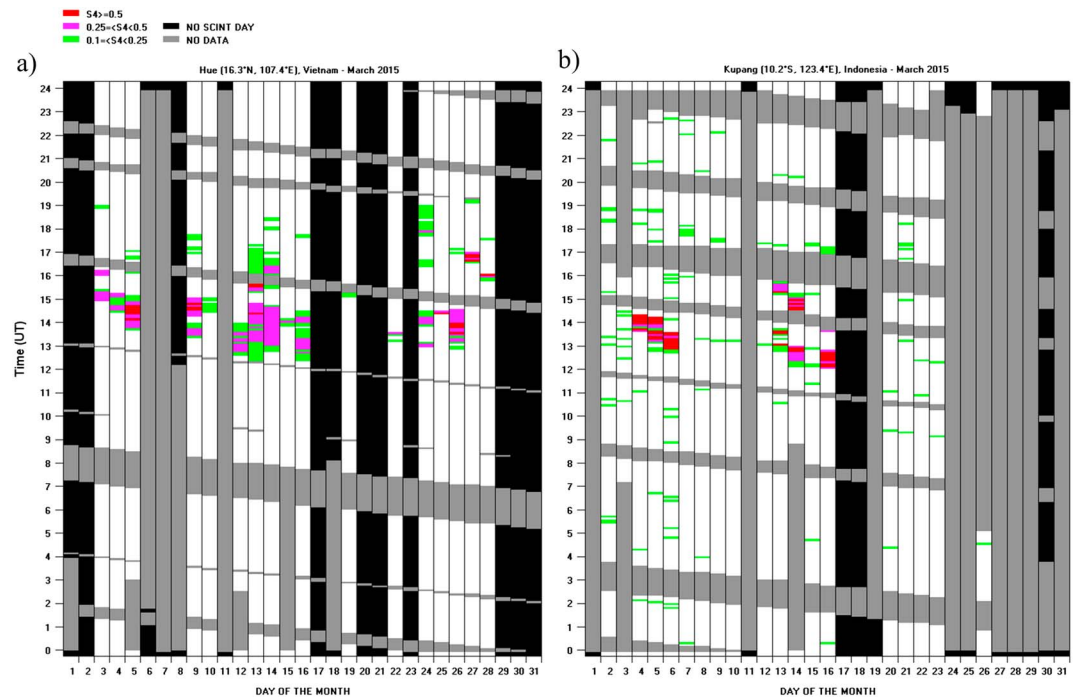


**Figure 14.** Scintillation occurrence in term of  $S_4$  at (a) Hue, Vietnam and (b) Kupang, Indonesia for March 2015. Red identifies the values of  $S_4$  greater than 0.5, violet identifies the values of  $S_4$  between 0.25 and 0.5, and green identifies the values of  $S_4$  between 0.1 and 0.25. Gray means data unavailability. Black highlights no scintillation days.

for scintillation are co-located, while the receiver in Hue is the closest to the Sanya ionosonde (distance is about 290 km). Similarly to *Alfonsi et al.* [2013], to equal the field of view of the GNSS receiver with the coverage of the vertical sounding, we apply an elevation angle mask of  $60^\circ$  on GNSS data. In Figure 14, scintillation levels are highlighted by colored rectangles. Red identifies the values of  $S_4$  greater than 0.5, violet identifies the values of  $S_4$  between 0.25 and 0.5, and green identifies the values of  $S_4$  in the range between 0.1 and 0.25. As in Figure 13, gray means data unavailability, while black highlights no scintillation days. Scintillation occurrence reflects the behavior observed for the spread  $F$ , as the occurrence of moderate to strong scintillation (total number of red and purple bins) is lower in Kupang than in Hue, although the former experiences the larger  $S_4$  intensity, as it is characterized by a larger number of red only bins. During the main and recovery phases, scintillation inhibition is present in both receivers. In general, the scintillation activity is inhibited or very low between 17 and 22.

The comparison between Figures 13 and 14 suggests that the ionosphere is more effective in producing amplitude scintillation (moderate to strong) when the quiet time uplift of the  $F$  layer takes place.

The different sizes of the ionospheric irregularities probed by HF and L-band signals clearly result by comparing spread  $F$  and scintillation occurrence on 19 March, when the scintillation occurrence is not associated to any presence of spread  $F$  irregularities.

### 5. Conclusions

In this paper, a characterization of the effects of Saint Patrick's Day storm over SEA has been provided by using a local network of GNSS receivers, magnetometers, and ionosondes.

Swarm satellite magnetic and ionospheric data have also been used to support the analysis in a scarcely investigated region.

The challenging complexity of the storm has been tackled successfully through a multidisciplinary approach. The changes in the formation and dynamics of the ionospheric irregularities during the stormy days are critically discussed, focusing on the RTI development and consequent enhancement/inhibition of the scintillation activity over SEA. This work aims at completing the picture of the 2015 Saint Patrick's Day storm,

nowadays available from current literature only at global level or in other geographical sectors. In particular, our work presents for the first time the comparison between northern and southern crests of the EIA in the SEA region.

Our study drives the following conclusions:

1. The inhibition of scintillation in the postsunset hours induced by the prompt penetration of electric field from auroral latitudes has been detected statistically, by considering data covering the entire month of March 2015. The picture drawn by means of the GBSC technique highlights that scintillation occurrence at postsunset is significantly reduced during the geomagnetically disturbed days but not reduced to zero. The enhancement (suppression) of the  $F$  layer uplift, prompting (impeding) the ionospheric irregularity formation, is not always present under disturbed geomagnetic conditions, hardening the prediction, and forecasting of the scintillations at low/equatorial latitudes.
2. Symmetries and asymmetries between the dynamics of EIA crests have been highlighted: the negative phase has been found to be more pronounced in the summer hemisphere than in the winter hemisphere.
3. The combined use of bottomside (manually scaled  $h'F$  from ionosondes), topside (electron density from Swarm), and integrated ( $vTEC$  from GNSS) ionospheric information highlights how the storm affects the  $F$  layer altitude and the consequent enhancement/suppression of the scintillations. Altitude of the  $F_2$  layer is the main factor responsible for the inhibition or triggering of irregularity formation in the plasma cascade under the gravity. The cascade is induced by the changes in the upward density gradient and is prompted by the westward electric field near sunset. When scintillation has been found to be inhibited, the irregularities embedded in plasma bubbles, produced in the above-mentioned cascade, do not likely reach scales below the Fresnel's one. This, then, confirms how the alternation of scintillation enhancement and inhibition is strongly linked with the  $F$  layer dynamics and irregularity scale sizes.
4. Differences in the western ( $108^\circ\text{E}$ – $111^\circ\text{E}$ ) and eastern ( $122^\circ\text{E}$ – $125^\circ\text{E}$ ) sectors of SEA have been found mainly in the trough region. The  $vTEC$  recovery to quiet values starts earlier in the western sector (21 March) than in the eastern one (22 March). Near the crests, the eastern sector seems to show larger mean  $\Delta TEC$  than the western one, starting from 22 March. This confirms the strong regional dependence of the storm development and the need of a regional assessment in depicting the effect of geomagnetic storms.
5. Although HF and L-band signals probe different sizes of the ionospheric irregularities, GNSS scintillation and spread  $F$  occurrences show similar patterns. Similarities and differences are highlighted in the paper. In particular, a significant difference is reported on 19 March, when the scintillation occurrence is not associated to any presence of spread  $F$  irregularities.

#### Acknowledgments

The authors thank the IGS Community for making available the GNSS data; the University of Massachusetts at Lowell for making available the GIRO data resources (<http://spase.info/SMWG/Observatory/GIRO>) and the SAO explorer program <http://ulcar.uml.edu/SAO-X/SAO-X.html>; the European Space Agency (ESA) mission team for the provision of the data, freely accessible at <https://earth.esa.int/web/guest/swarm/data-access>; and the Kyoto World Data Center for Geomagnetism for the provision of  $Dst$  data (<http://wdc.kugi.kyoto-u.ac.jp/dstdir/index.html>). The ERICA project was funded under the Alcantara framework, one of the General Studies Programme carried on by the European Space Agency (ESA). The authors are grateful to Luigi (Gg) Ciraolo for its valuable help in TEC calibration.

#### References

- Aarons, J. (1991), The role of the ring current in the generation or inhibition of equatorial  $F$  layer irregularities during magnetic storms, *Radio Sci.*, *26*(4), 1131–114, doi:10.1029/91RS00473.
- Alfonsi, L., L. Spogli, G. De Franceschi, V. Romano, M. Aquino, A. Dodson, and C. N. Mitchell (2011a), Bipolar climatology of GPS ionospheric scintillation at solar minimum, *Radio Sci.*, *46*, RS0D05, doi:10.1029/2010RS004571.
- Alfonsi, L., L. Spogli, J. R. Tong, G. De Franceschi, V. Romano, A. Bourdillon, and C. N. Mitchell (2011b), GPS scintillation and TEC gradients at equatorial latitudes in April 2006, *Adv. Space Res.*, *47*(10), 1750–1757, doi:10.1016/j.asr.2010.04.020.
- Alfonsi, L., L. Spogli, M. Pezzopane, V. Romano, E. Zuccheretti, G. De Franceschi, M. A. Cabrera, and R. G. Ezquer (2013), Comparative analysis of spread- $F$  signature and GPS scintillation occurrences at Tucumán, Argentina, *J. Geophys. Res. Space Physics*, *118*, 4483–4502, doi:10.1002/jgra.50378.
- Amory-Mazaudier, C., et al. (2006), Sun–Earth system interaction studies over Vietnam: An international cooperative project, *Ann. Geophys.*, *24*, 3313–3327, doi:10.5194/angeo-24-3313-2006.
- Astafeyeva, E., I. Zakharenkova, and E. Doornbos (2015a), Opposite hemispheric asymmetries during the ionospheric storm of 29–31 August 2004, *J. Geophys. Res. Space Physics*, *120*, 697–714, doi:10.1002/2014JA020710.
- Astafeyeva, E., I. Zakharenkova, and M. Forster (2015b), Ionospheric response to the 2015 St. Patrick's day storm: A global multi-instrumental overview, *J. Geophys. Res. Space Physics*, *120*, 9023–9037, doi:10.1002/2015JA026229.
- Basu, S., K. M. Groves, S. Basu, and P. J. Sultan (2002), Specification and forecasting of scintillations in communication/navigation links: Current status and future plans, *J. Atmos. Sol. Terr. Phys.*, *64*, 1745–1754, doi:10.1016/S1364-6826(02)00124-4.
- Bibl, K., and B. W. Reinisch (1978), The universal digital ionosonde, *Radio Sci.*, *13*, 519–530, doi:10.1029/RS013i003p00519.
- Booker, H. G., and H. W. Wells (1938), Scattering of radio waves by the  $F$ -region of the ionosphere, *J. Geophys. Res.*, *43*, 249–256, doi:10.1029/TE043i003p00249.
- Buonsanto, M. J. (1999), Ionospheric storms—A review, *Space Sci. Rev.*, *88*, 563–601, doi:10.1023/A:1005107532631.
- Carter, B. A., E. Yizengaw, R. Pradipta, J. M. Retterer, K. Groves, C. Valladares, R. Caton, C. Bridgwood, R. Norman, and K. Zhang (2016), Global equatorial plasma bubble occurrence during the 2015 St. Patrick's Day storm, *J. Geophys. Res. Space Physics*, *121*, 894–905, doi:10.1002/2015JA022194.
- Cesaroni, C. (2015), A multi instrumental approach to the study of equatorial ionosphere over South America, PhD dissertation, University "Alma Mater studiorum", Bologna, Italy, doi:10.6092/unibo/amsdottorato/6889.

- Cesaroni, C., C. Scotto, and A. Ippolito (2013), An automatic quality factor for Autoscala  $f_oF_2$  values, *Adv. Space Res.*, *51*(12), 2316–2321, doi:10.1016/j.asr.2013.02.009.
- Cesaroni, C., L. Spogli, L. Alfonsi, G. De Franceschi, L. Ciralo, J. F. G. Monico, C. Scotto, V. Romano, M. Aquino, and B. Bougard (2015), L-band scintillations and calibrated total electron content gradients over Brazil during the last solar maximum, *J. Space Weather Space Clim.*, *5*, A36, doi:10.1051/swsc/2015038.
- Chen, W. S., C. C. Lee, J. Y. Liu, F. D. Chu, and B. W. Reinisch (2006), Digisonde spread  $F$  and GPS phase fluctuations in the equatorial ionosphere during solar maximum, *J. Geophys. Res.*, *111*, A12305, doi:10.1029/2006JA011688.
- Ciralo, L., F. Azpilicueta, C. Brunini, A. Meza, and S. M. Radicella (2007), Calibration errors on experimental slant total electron content (TEC) determined with GPS, *J. Geod.*, *81*(2), 111–120.
- Dabas, R. S., L. Singh, D. R. Lakshmi, P. Subramanyam, P. Chopra, and S. C. Garg (2003), Evolution and dynamics of equatorial plasma bubbles: Relationships to  $E \times B$  drift, postsunset total electron content enhancements and equatorial electrojet strength, *Radio Sci.*, *38*(4), 1075, doi:10.1029/2001RS002586.
- de Rezende, L. F. C., E. R. de Paula, I. S. Batista, I. J. Kantor, and M. T. H. Muella (2007), Study of ionospheric irregularities during intense magnetic storms, *Rev. Bras. Geof.*, *25*(Supl 2), 151–158.
- Foster, M. P., and A. N. Evans (2008), An evaluation of interpolation techniques for reconstructing ionospheric TEC maps, *IEEE Trans. Geosci. Remote Sens.*, *46*(7), 2153–2164, doi:10.1109/TGRS.2008.916642.
- Friis-Christensen, E., H. Lühr, D. Knudsen, and R. Haugmans (2008), Swarm—An Earth observation mission investigating geospace, *Adv. Space Res.*, *41*(1), 210–216, doi:10.1016/j.asr.2006.10.008.
- Fuller-Rowell, T. J., M. V. Codrescu, H. Risbeth, R. J. Moffett, and S. Quegan (1996), On the seasonal response of the thermosphere and ionosphere to geomagnetic storms, *J. Geophys. Res.*, *101*, 2343–2354, doi:10.1029/95JA01614.
- Galkin, I. A., and B. W. Reinisch (2008), The new ARTIST 5 for all digisondes, Ionosonde Network Advisory Group Bulletin 69, 8 pp. [Available at: <http://www.ips.gov.au/IPSHosted/INAG/web-69/2008/artist5-inag.pdf>]
- Goncharenko, L. P., J. C. Foster, A. J. Coster, C. Huang, N. Aponte, and L. J. Paxton (2007), Observations of a positive storm phase on September 10, 2005, *J. Atmos. Sol. Terr. Phys.*, *69*, 1253–1272, doi:10.1016/j.jastp.2006.09.011.
- Huang, C.-S. (2009), Eastward electric field enhancement and geomagnetic positive bay in the dayside low-latitude ionosphere caused by magnetospheric substorms during sawtooth events, *Geophys. Res. Lett.*, *36*, L18102, doi:10.1029/2009GL040287.
- Huang, C.-S. (2012), Statistical analysis of dayside equatorial ionospheric electric fields and electrojet currents produced by magnetospheric substorms during sawtooth events, *J. Geophys. Res.*, *117*, A02316, doi:10.1029/2011JA017398.
- Jin, S. G., O. Luo, and P. Park (2008), GPS observations of the ionospheric  $F_2$ -layer behavior during the 20th November 2003 geomagnetic storm over South Korea, *J. Geod.*, *82*(12), 883–892, doi:10.1007/s00190-008-0217-x.
- Jose, L., S. Ravindran, C. Vineeth, T. K. Pant, and S. Alex (2011), Investigation of the response time of the equatorial ionosphere in context of the equatorial electrojet and equatorial ionization anomaly, *Ann. Geophys.*, *29*, 1267–1275, doi:10.5194/angeo-29-1267-2011.
- Kelley, M. C. (2009), *The Earth's Ionosphere: Plasma Physics and Electrodynamics*, *Int. Geophys. Ser.*, vol. 96, pp. 556, Elsevier.
- Kintner, P. M., T. Humphreys, and J. Hinks (2009), GNSS and ionospheric scintillation, *Inside GNSS*, *4*(4), 22–30.
- Knudsen, D., J. Burchill, S. Buchert, I. Coco, L. Toffner-Clausen, and P. E. Holmdahl Olsen (2015), Swarm preliminary plasma dataset user note, ESA Ref. SWAM-GSEG-EOPG-TN-15-0003. [Available at <https://earth.esa.int/web/guest/document-library/browse-document-library/-/article/swarm-preliminary-plasma-dataset-user-note>]
- MacDougall, J. W., I. F. Grant, and X. Shen (1995), The Canadian advanced digital ionosonde: Design and results URSI INAG Ionospheric Station Inf. Bulletin, UAG-104.
- Mannucci, A. J., B. D. Wilson, and C. D. Edwards (1993), A new method for monitoring the Earth ionosphere total electron content using the GPS global network paper presented at ION GPS 93, Inst. Of Navig., Salt Lake City, Utah.
- Mayaud, P. N. (1980), *Derivation, Meaning, and Use of Geomagnetic Indices*, *Geophys. Monogr. Ser.*, vol. 22, pp. 607, AGU, Washington, D. C.
- Muella, M. T. A. H., E. A. Kherani, E. R. de Paula, A. P. Cerruti, P. M. Kintner, I. J. Kantor, C. N. Mitchell, I. S. Batista, and M. A. Abdu (2010), Scintillation-producing Fresnel-scale irregularities associated with the regions of steepest TEC gradients adjacent to the equatorial ionization anomaly, *J. Geophys. Res.*, *115*, A03301, doi:10.1029/2009JA014788.
- Nava, B., J. Rodríguez-Zuluaga, K. Alazo-Cuartas, A. Kashcheyev, Y. Migoya-Orué, S. M. Radicella, C. Mory-Mazaudier, and R. Fleury (2016), Middle- and low-latitude ionosphere response to 2015 St. Patrick's Day geomagnetic storm, *J. Geophys. Res. Space Physics*, *121*, 3421–3438, doi:10.1002/2015JA022299.
- Nayak, C., L.-C. Tsai, S.-Y. Su, I. A. Galkin, A. T. K. Tan, E. Nofri, and P. Jamareegulgarn (2016), Peculiar features of the low-latitude and midlatitude ionospheric response to the St. Patrick's Day geomagnetic storm of 17 March 2015, *J. Geophys. Res. Space Physics*, *121*, 7941–7960, doi:10.1002/2016JA022489.
- Ngwira, C. M., G. K. Seemala, and J. B. Habarulema (2013), Simultaneous observations of ionospheric irregularities in the African low-latitude region, *J. Atmos. Sol. Terr. Phys.*, *97*, 50–57, doi:10.1016/j.jastp.2013.02.014.
- Novatel (2012), GPStation-6 GNSS Ionospheric Scintillation and TEC Monitor (GISTM) receiver user manual, NovAtel Inc., Calgary, Alberta. [Available at <http://www.novatel.com/assets/Documents/Manuals/om-20000132.pdf>, Accessed date 6 July 2016.]
- Pedatella, N., C. Stolle, and J. Chau (2015), Comparing Swarm electron density data to COSMIC GPS radio occultation observations paper presented at the 26<sup>th</sup> IUGG General Assembly, Prague, Czech Republic, June 22–July 2 2015.
- Pezzopane, M. (2004), Interpret: A Windows software for semiautomatic scaling of ionospheric parameters from ionograms, *Comput. Geosci.*, *30*, 125–130, doi:10.1016/j.cageo.2003.09.009.
- Pezzopane, M., and C. Scotto (2007), The automatic scaling of critical frequency  $f_oF_2$  and MUF(3000)F<sub>2</sub>: A comparison between Autoscala and ARTIST 4.5 on Rome data, *Radio Sci.*, *42*, RS4003, doi:10.1029/2006RS003581.
- Pezzopane, M., and C. Scotto (2010), Highlighting the  $F_2$  trace on an ionogram to improve Autoscala performance, *Comput. Geosci.*, *36*, 1168–1177, doi:10.1016/j.cageo.2010.01.010.
- Piggott, W. R., and K. Rawer (1972), *URSI Handbook of Ionogram Interpretation and Reduction*, 2nd ed., pp. 325, Elsevier, New York.
- Pignalberi, A., M. Pezzopane, R. Tozzi, P. Michelis, and I. Coco (2016), Comparison between IRI and preliminary Swarm Langmuir probe measurements during the St. Patrick storm period, *Earth Planets Space*, *68*(1), 1–18, doi:10.1186/s40623-016-0466-5.
- Povero, G., et al. (2015), Ionosphere monitoring in South East Asia: Activities in GINESTRA and ERICA projects, in *2015 International Association of Institutes of Navigation World Congress (IAIN)*, pp. 1–7, IEEE, New York.
- Prikryl, P., et al. (2015), GPS phase scintillation at high latitudes during geomagnetic storms of 7–17 March 2012—Part 2: Interhemispheric comparison, *Ann. Geophys.*, *33*(6), 657–670, doi:10.5194/angeo-33-657-2015.
- Pröls, G. W. (1995), Ionospheric  $F$ -region storms, in *Handbook of Atmospheric Electrodynamics*, vol. 2, edited by H. Volland, pp. 195–248, CRC Press, Boca Raton, Fla.

- Rangarajan, G. K. (1989), Indices of geomagnetic activity, in *Geomagnetism*, edited by J. A. Jacobs, pp. 323, Academic Press, London.
- Reinisch, B. W., and I. A. Galkin (2011), Global Ionospheric Radio Observatory (GIRO), *Earth Planets Space*, *63*, 377–381, doi:10.5047/eps.2011.03.001.
- Reinisch, B. W., I. A. Galkin, G. Khmyrov, A. Kozlov, and D. F. Kitrosser (2004), Automated collection and dissemination of ionospheric data from the Digisonde network, *Adv. Radio Sci.*, *2*, 241–247, doi:10.5194/ars-2-241-2004.
- Rino, C. L. (1979), A power law phase screen model for ionospheric scintillation: 1. Weak scatter, *Radio Sci.*, *14*, 1135–1145, doi:10.1029/RS014i006p01135.
- Rishbeth, H. (1971), Polarization fields produced by winds in the equatorial *F* region, *Planet. Space Sci.*, *19*, 357–369, doi:10.1016/0032-0633(71)90098-5.
- Sastri, J. H., Y. Kamide, and K. Yumoto (2003), Signatures for magnetospheric substorms in the geomagnetic field of dayside equatorial region: Origin of the ionospheric component, *J. Geophys. Res.*, *108*(A10), 1375, doi:10.1029/2003JA009962.
- Spogli, L., L. Alfonsi, G. De Franceschi, V. Romano, M. H. O. Aquino, and A. Dodson (2009), Climatology of GPS ionospheric scintillations over high and mid-latitude European regions, *Ann. Geophys.*, *27*(9), 3429–3437, doi:10.5194/angeo-27-3429-2009.
- Spogli, L., L. Alfonsi, V. Romano, G. De Franceschi, G. M. J. Francisco, M. H. Shimabukuro, B. Bougard, and M. Aquino (2013a), Assessing the GNSS scintillation climate over Brazil under increasing solar activity, *J. Atmos. Sol.-Terr. Phys.*, *105*, 199–206, doi:10.1016/j.jastp.2013.10.003.
- Spogli, L., L. Alfonsi, L. Cilliers, E. Correia, G. De Franceschi, C. N. Mitchell, V. Romano, J. Kinrade, and M. A. Cabrera (2013b), GPS scintillations and total electron content climatology in the southern low, middle and high latitude regions, *Ann. Geophys.*, *56*(2), 0220, doi:10.4401/ag-6240.
- Tulasi Ram, S., et al. (2016), Duskside enhancement of equatorial zonal electric field response to convection electric fields during the St. Patrick's Day storm on 17 March 2015, *J. Geophys. Res. Space Physics*, *121*, 538–548, doi:10.1002/2015JA021932.
- Van Dierendonck, A. J., J. Klobuchar, and Q. Hua (1993), Ionospheric scintillation monitoring using commercial single frequency C/A code receivers, in *ION GPS-93 Proceedings of the Sixth International Technical Meeting of the Satellite Division of the Institute of Navigation*, pp. 1333–1342, Salt Lake City, UT.
- Vanlommel, P. (2015), STCE newsletter: Issue 27 March 2015. [Available at: <http://www.stce.be/newsletter/pdf/2015/STCEnews20150327.pdf>. Access 6 July 2016.]
- Wernik, A. W., and C. H. Liu (1974), Ionospheric irregularities causing scintillations of GHz frequency radio signals, *J. Atmos. Terr. Phys.*, *36*, 871–879, doi:10.1016/0021-9169(74)90032-4.
- Wernik, A. W., J. A. Secan, and E. J. Fremouw (2003), Ionospheric irregularities and scintillation, *Adv. Space Res.*, *31*(4), 971–981, doi:10.1016/S0273-1177(02)00795-0.
- Yizengaw, E., M. B. Moldwin, A. Komjathy, and A. J. Mannucci (2006), Unusual topside ionospheric density response to the November 2003 superstorm, *J. Geophys. Res.*, *111*, A02308, doi:10.1029/2005JA011433.
- Young, E. R., W. J. Burke, F. J. Rich, and R. C. Sagalyn (1984), The distribution of topside spread *F* from in situ measurements by Defense Meteorological Satellite Program: *F*<sub>2</sub> and *F*<sub>s</sub>, *J. Geophys. Res.*, *89*, 5565–5573, doi:10.1029/JA089iA07p05565.
- Zhong, J., W. Wang, X. Yue, A. G. Burns, X. Dou, and J. Lei (2016), Long-duration depletion in the topside ionospheric total electron content during the recovery phase of the March 2015 strong storm, *J. Geophys. Res. Space Physics*, *121*, 4733–4747, doi:10.1002/2016JA022469.